Effects of Land-Surface-Vegetation on the boreal summer surface climate of a GCM

Andrea Alessandri[1], Silvio Gualdi[1], Jan Polcher[2], and Antonio Navarra[1]

[1]National Institute of Geophysics and Volcanology, Bologna, Italy
[2]Institute Pierre and Simone Laplace, Paris, France

Manuscript submitted to

Journal of Climate

December 22, 2006

[0]*Correspondence to:* Andrea Alessandri
National Institute of Geophysics and Volcanology
Via Creti,12
I-40128 Bologna, Italy
e-mail alessandri@bo.ingv.it
Phone +39 051 4151451
Fax +39 051 4151499

Abstract

A Land Surface Model (LSM) has been included in the ECHAM4 Atmospheric General Circulation Model (AGCM). The LSM is an early version of ORCHIDEE (Organizing Carbon and Hydrology In Dynamic EcosystEms) and it replaces the simple land surface scheme previously included in ECHAM4. The purpose of this paper is to document how a more exhaustive consideration of the land-surface-vegetation processes affects the simulated boreal summer surface climate.

In order to investigate the impacts on the simulated climate, different sets of AMIP-type simulations have been performed with Echam4 alone and with the AGCM coupled with ORCHIDEE. Furthermore, to assess the effects of the increase in horizontal resolution the coupling of Echam4 with the LSM has been implemented at different horizontal resolutions.

The analysis reveals that the LSM has large effects on the simulated boreal summer surface climate of the atmospheric model. Considerable impacts are found in the surface energy balance due to changes in the surface latent heat fluxes over tropical and mid-latitude areas covered with vegetation. Rainfall and atmospheric circulation are substantially affected by these changes. In particular, increased precipitation is found over evergreen and summergreen vegetated areas.

Due to the socio-economical relevance, particular attention has been devoted to the Indian Summer Monsoon (ISM) region. Our results indicate that precipitation over the Indian subcontinent is better simulated with the coupled Echam4-ORCHIDEE model compared to the atmospheric model alone.

1 Introduction

Over the last decades both model and observational studies have shown that the climate system is sensitive to the processes that characterize the Earth's continental surface and that an accurate representation of these processes in climate models is of great importance. Early numerical sensitivity experiments conducted in the 80s, showed that changes in surface albedo (e.g: Charney et al., 1977), soil humidity (Shukla and Mintz, 1982; Meehl and Washington, 1988) and surface roughness length (Sud et al., 1988) have a considerable impact on atmospheric circulation and precipitation patterns. Since that time, numerical models have continously improved, with the inclusion of more and more realistic land surface schemes and with wider inclusion of vegetation functions and characteristics.

A parameterization of the vegetation included in an AGCM permits to better simulate the evolution of surface parameters such as roughness length, albedo and surface-soil moisture. Furthermore, the inclusion of a realistic vegetation allows a description of the function of roots, of the physiological control of transpiration and of the water interception by the vegetation canopies which is quickly evaporated back to the atmosphere. This last process, also known as "interception water loss", can be very important for a realistic estimate of the evapotranspiration rate over vegetation covered areas, as shown by Stewart (1977). Using an individual pine species, he showed that, for that particular vegetation species, the rate of evaporation of intercepted water can be as high as three times the rate of transpiration under the same atmospheric, surface and radiation conditions (Stewart, 1977).

The idea that vegetation influences climate is hardly new. Apparently, Christopher Columbus is reported to have believed that heavy rainfall in the New World was caused by the rank forest vegetation (Kittredge, 1948; Thompson , 1980; Bonan, 2002). The main mechanism by which vegetation is supposed to act to modify the precipitation intensity is through a positive feedback between evapotranspiration and rainfall. Shukla and Mintz (1982) conducted a sensitivity numerical GCM experiment in which two different and opposite constraints were placed upon the land surface evapotranspiration. In the first

one, no evapotranspiration was allowed, while in the second one evapotranspiration was set equal to the model simulated potential evapotranspiration (i.e.: the maximum possible evapotranspiration for the given atmospheric condition, which is computed assuming that the soil is saturated with water). They found that, in the GCM climate, "the global fields of rainfall, temperature and motion strongly depend on the land-surface evapotranspiration". However, the connection between evapotranspiration and precipitation depends on a large number of interacting thermodynamic and dynamical processes. As stated by Shukla and Mintz (1982), reduction or increase in evapotranspiration does not necessarily mean a reduction or an increase in precipitation, but the exact response will vary from region to region, depending on how the large-scale circulation is modified. Whether or not the increased moisture supply from the surface is able to produce stronger precipitation, and possibly feedback with the convective activity, depends on the background stability conditions in the boundary layer due to the atmospheric circulation (e.g: Barros and Wenje, 2002).

During the 90s, a series of numerical experiments aimed to assess the impacts of tropical deforestation have been performed (e.g: Henderson-Sellers et al., 1993; Dirmeyer and Shukla, 1994; Polcher and Laval, 1994; McGuffie et al., 1995). These experiments showed a strong sensitivity of simulated climate to tropical deforestation. However, the deforestation experiments showed also a large model dependence, most likely due to the difference in the GCM dynamical structures, land-surface representation, ocean description and experimental design.

Recent modeling and observational studies further indicate that land surface and vegetation can considerably feed back on climate (e.g: Bonan, 2002; Kaufmann et al., 2003; Knorr and Schnitzler, 2006), suggesting that the feedbacks between land surface and atmosphere could be important determinants of climate at a range of spatial (local to global) and temporal scales (seasonal to centennial and longer). Lawrence and Slingo (2004) (van den Hurk et al., 2003) showed that the introduction of vegetation (LAI) seasonality into the Met Office Hadley Centre Unified Model (the European Centre for Medium-Range

Weather Forecasts model) increases surface evaporation seasonal cycle over land and that this is able to produce enhanced growing season precipitation rates where the simulated latent heat flux (evaporation) increase is large. Koster et al. (2002, 2003) and Koster and Suarez (2004) using both numerical model experiments and observational evidences, suggested that land surface-atmosphere feedbacks can strongly influence the precipitation on regional scale. In a more recent work, Koster et al. (2004) evidenced that the strongest potential impact on the boreal summer precipitation variability, due to soil moisture anomalies, is found in transition zones between wet and dry climates, such as in the central Great Plains of North America, the Sahel, central Africa and India. The results of a further numerical study by Schubert et al. (2004), indicate that the dramatic 1930s Dust Bowl drought that occurred in the southern Great Plains was caused by anomalous tropical sea surface temperature during that decade and that interactions between the atmosphere and the land surface considerably increased its severity.

The Asian summer monsoon has been largely studied, also because of the impacts that this phenomenon has on the economy of one of the most populated region of the world. Some works suggest that land surface processes have very important influence on the Asian summer monsoon but the extent and the mechanism of such effects are still not completely understood. Yang and Lau (1998) conducted a series of model experiments aimed to understand the influences of sea surface temperature (SST) and land surface processes on the Asian Summer monsoon. They concluded that land surface processes mainly affect the early stage of the monsoon and that land surface variations reinforce the monsoon anomalies produced by warm SST forcing. Lau and Bua (1998) proposed a monsoon land-atmosphere feedback mechanism operating when the evapotranspiration from the surface is below the potential rate (e.g: onset phase of the monsoon). Following this mechanism, an increase in evapotranspiration is able to further moisten and destabilize the atmospheric boundary layer triggering the rapid growth of deep convection and precipitation. The tropospheric air, warmed by the latent heat release, rises leading to increased low level moisture convergence which in turn reinforces the convective activ-

ity. As a result there will be a further increase in moisture availability at the surface for evapotranspiration.

The main objective of this work is the study of the effects of a more exhaustive consideration of the land surface and vegetation processes on the simulated surface climate of the Echam4 (EcmwfHAMburg version 4) AGCM. An early version of ORCHIDEE (Organizing Carbon and Hydrology In Dynamic EcosystEms) has been included in Echam4. The coupling between the LSM and the atmospheric component has been achieved by virtue of a fully implicit coupling numerical scheme. ORCHIDEE replaces the simple land surface scheme included in Echam4 which uses a semi-implicit coupling numerical scheme at the interface surface-atmosphere. The effects of an improved representation of the land surface and vegetation on the boreal summer surface climate simulated by Echam4 have been analyzed in detail. An assessment of the sensitivity of the results with respect to the increased model horizontal resolution and to the coupling numerical scheme has been performed as well.

The work is organized as follows: section 2 describes briefly the Echam4 atmospheric GCM and the early version of ORCHIDEE used for the present work. Section 3 describes the experiments performed as well as the reanalysis and observation datasets used in order to make a comparison with the results of the models. Section 4 is dedicated to the results and it is essentially divided in 3 parts: subsection 4.1 evaluates the vegetation representation of the Echam4-ORCHIDEE (EchOrc) model. In subsection 4.2, the assessment of the major impacts, due to the coupling with ORCHIDEE, on the boreal summer surface climate simulated by Echam4 at coarse resolution is discussed. Subsection 4.3 analyses the sensitivity of the results due to the coupling numerical scheme and to the increase in horizontal resolution. Finally, section 5 contains the conclusions of this study.

2 The models

2.1 The Echam4 GCM

Echam4 is the fourth generation of the ECHAM atmospheric general circulation model developed at the Max Planck Institut Für Meteorologie in Hamburg. The model equations are solved on 19 hybrid vertical levels (top at 10 hPa) by using the spectral transform method. In this work, Echam4 is used with a triangular truncation T30, which corresponds to an associated gaussian grid of approximately $3.75^\circ \times 3.75^\circ$ in latitude and longitude. Two simulations were also performed with a triangular truncation T106 (i.e., corresponding to an associated gaussian grid of about $1.125^\circ \times 1.125^\circ$), in order to investigate the effects of the horizontal resolution. The time step for dynamics and physics is set at 1800 sec for the T30 horizontal resolution and at 720 sec for the T106 case. These numbers are chosen to get a numerical stability, following the Courant-Friedrichs-Levy (CFL) criterion (Roeckner et al., 1992). An exhaustive and detailed description of the dynamical and physical structure as well as of the simulated climatology of the model has been given by Roeckner et al. (1996).

2.1.1 Echam4 surface parameterizations

In the Echam model (Roeckner et al., 1992, 1996), the surface fluxes of momentum, heat, and moisture are calculated according to the classical aerodynamic formulas using the Monin-Obukhov similarity theory (e.g: Stull, 1997):

$$F_x = \rho C_D |v| (X_a - X_S) \tag{1}$$

where ρ is the density of air, C_D is the drag coefficient and $|v|$ is the absolute value of the horizontal wind speed. The value of X_a may be identified with the atmospheric value, at the model level closest to the surface, of one of the quantities that are subject to the turbulent exchange (momentum, heat and humidity), while X_S is the surface value. For evaluating the moisture flux over land, each grid element is divided into four fractions.

These fractions are snow cover, wet skin fraction, vegetation and bare soil. The representation of the vegetation uses an aggregated treatment of the canopy characteristics (i.e: without taking into account any information on the vegetation diversity within the grid box). The vegetation characteristics are provided, for each grid box, by means of mean prescribed constant climatological values for parameters like surface roughness length and albedo (Roeckner et al., 1996). The moisture flux is calculated for each of the four fractions according to the following equation:

$$E = \rho C_h |v| \beta (q_a - h q_s(T_s, p_s)), \tag{2}$$

where q_s is the saturation-specific humidity , T_s the temperature and p_s the pressure at the surface, whereas q_a is the atmospheric specific humidity at a reference level. The values of the "beta coefficient" (β) and of h, which represent the limitation to the evaporation due to soil moisture availability, have to be specified for each fraction.

The coupling between the land surface and the vertical diffusion is performed using a semi-implicit coupling scheme with a Dirichlet closure at the interface. The calculation of the soil temperature is based on the heat diffusion through soil layers. For this purpose, the heat conduction equation is solved for five layers over land and land ice, following Warrilow et al. (1986). The water budget within the soil is represented by means of a single layer (bucket model) following Manabe (1969). The storage capacity of this single layer soil is spatially varying and prescribed following a global dataset of estimated total water-holding capacities (Patterson, 1990). In a simple bucket model, surface runoff is produced by the overflow that occurs when the soil water reservoir is saturated.

2.2 ORCHIDEE

ORCHIDEE (Organizing Carbon and Hydrology In Dynamic EcosystEms; Krinner et al., 2005) is a surface-dynamic vegetation-atmosphere transfer model developed at IPSL in Paris. The version of ORCHIDEE used for this work is an early version of the model and it does not contain the parameterizations of vegetation and carbon dynamics. In the version used, the vegetation distribution is prescribed and the Leaf Area Index (LAI) is

diagnosed as a function of temperature (Polcher, 1994). The effective vegetation cover and the biophysical state of the vegetation are defined by the LAI (see section 2.3) through which a number of other biophysical vegetation variables such as albedo and roughness length are derived interactively.

Transpiration and direct evaporation of water stored in the canopy interception reservoir are computed using twelve Plant Functional Types (PFTs, see Table 1) that may be present simultaneously in one grid element (besides bare soil). The moisture flux is calculated separately for each fractional surface cover class, and the total flux for each grid box is determined as an area-weighted average, thus taking into account the relative fractional coverage of the vegetation types. The evapotranspiration is controlled by the aerodynamic resistance, the architectural resistance (resistance between the leaves and the canopy top), which is a function of vegetation type, and the canopy resistance. The formulation of the canopy resistance is defined as follows:

$$r_c = \frac{1}{LAI}\left(\frac{R_S + R_{S0}}{R_S}\right)\left(\frac{a + \lambda\delta c}{k_0}\right) \tag{3}$$

where R_S is the incident solar radiation at the land surface, R_{S0} is the half light saturation factor, δc is the water vapor concentration deficit and a, λ and k_0 are parameters entering in the function of water vapor concentration deficit.

The energy and water exchanges between the atmosphere and the surface and the soil water budget are taken from SECHIBA (Schématisation des Echanges Hydriques à l'Interface Biosphère-Atmosphère; Ducoudré et al., 1993; de Rosnay and Polcher, 1998). The soil temperature is computed similarly to what described for Echam4, using the heat diffusion through soil layers. Differently from Echam4, in ORCHIDEE the heat diffusion has been implemented with a discretization in seven soil layers instead of five.

The soil water is stored in two conceptual layers with variable depths (Ducoudré et al., 1993). If the soil is dry and it starts raining, an upper moisture layer is created from the top to the bottom of the soil. When evapotranspiration is larger than precipitation, water is removed from the closest level where it is available in the soil. First, the soil moisture is depleted from the the upper layer, again from the top to the bottom, until

the upper reservoir disappears. Then evaporation continues from the lower layer. The upper reservoir can deepen when it is saturated until the total soil water content reaches its maximum storage capacity. In this latter case the upper reservoir disappears and all the water in the soil goes to the lower reservoir, which then extends through the entire soil column. The total depth of the soil is 2 meters and it is constant throughout the continents. On the other hand, the storage capacity is a function of the land cover types. In vegetation covered areas the storage capacity is prescribed as $150mm$ water for each meter of soil depth while bare soils have a reduced water storage capacity of $30mm$ for each meter of soil depth.

2.3 The LAI and effective vegetation cover computation

In the version of ORCHIDEE used here, the LAI of herbaceous and deciduous PFTs is computed as a function of soil temperature (T_c) at specific depth, different for each PFT. LAI is computed as a function of the squared difference between the actual soil temperature and the optimal growing temperature value, which is prescribed for each PFT:

$$LAI = lai_{min,iPFT} + tempf(T_c)(lai_{max,iPFT} - lai_{min,iPFT}) \tag{4}$$

where $tempf$ is defined as follows:

$$tempf = 1 - zfact(Temp_{opt,iPFT} - T_c)^2 \tag{5}$$

and with $zfact = \frac{1}{(Temp_{opt,iPFT} - Temp_{min,iPFT})^2}$

In the previous equations $lai_{min,iPFT}$ ($lai_{max,iPFT}$) is the minimum (maximum) value of LAI for each PFT; $Temp_{min,iPFT}$ is the minimum temperature which makes possible the growth of that PFT; $Temp_{opt,iPFT}$ is the temperature which permits the optimal growing of that particular PFT. In the case of evergreen PFTs, the average between the lower and maximum LAI value is prescribed.

The effective fractional vegetation cover for each PFT (v_{iPFT}) is calculated as follows:

$$v_{iPFT} = v_{max,iPFT}(1 - e^{-kLAI_{iPFT}}) \tag{6}$$

where $k = 0.5$ and $v_{max,iPFT}$ is the prescribed maximum vegetation cover. For each PFT $\frac{v_{iPFT}}{v_{max,iPFT}}$ represents the fraction of vegetated areas effectively covered by canopies.

2.4 Surface albedo representation

In ORCHIDEE the distinction between visible (vis) and near-infrared (nir) radiation is considered. The total surface albedo, for each spectral band, is computed as the weighted average of the various PFT cover albedo ($albedo_{i,vis,nir}$), the bare soil albedo ($albedo_{soil}$) and the snow cover albedo($albedo_{snow}$):

$$albedo_{tot,vis,nir} = \sum_i veget_i \cdot albedo_{i,vis,nir} + f \cdot albedo_{soil,vis,nir} + \beta \cdot albedo_{snow,vis,nir} \quad (7)$$

where $veget_i$, f and β are the fractions, for each grid element, of vegetation cover for the ith PFT, of bare soil and snow cover respectively. The soil albedo is function of the soil humidity and is represented by the following linear equation:

$$albedo_{soil,vis,nir} = albedo_{wet,vis,nir} + hdry \cdot (albedo_{dry,vis,nir} - albedo_{wet,vis,nir}) \quad (8)$$

here, $albedo_{dry,vis,nir}$ and $albedo_{wet,vis,nir}$ are the maximum value corresponding to dry conditions and the minimum value corresponding to wet soil conditions; $hdry$ is a function of upper soil aridity: $hdry = 1$ if the upper soil layer is completely dry and $hdry = 0$ if the upper soil layer is saturated with water. The albedo over snow covered areas is represented following Chalita and LeTreut (1994).

2.5 The implicit coupling between Echam4 and ORCHIDEE

Following Polcher et al. (1998), the coupling has been performed with a fully implicit numerical scheme which ensures for energy conservation at the surface-atmosphere interface. The coupling of the LSM to the vertical diffusion has been implemented with a "Neumann closure" at the interface. This kind of coupling requires that fluxes are exchanged between the land and the atmosphere. This leads to more complex computations within the land surface scheme than what would be needed for the "Dirichlet closure". In the latter case, in fact, only the state variables are exchanged at the interface.

3 Experiments and data

3.1 Experiments performed

Two sets of simulations, with prescribed observed sea surface temperature (SST) forcing (AMIP-type experiments) have been performed with the Echam4 AGCM (control experiment) and with Echam4 coupled with ORCHIDEE (EchOrc). The prescribed SST has been obtained from the HadISST1.1 Global Sea-Ice and Sea-Surface Temperature dataset for the period 1956-1999. An ensemble of three simulations has been generated with both Echam4 and EchOrc at T30 resolution, using different initial conditions for each ensemble member. In order to test how the results are affected by the horizontal resolution of the model, two further simulations with Echam4 and EchOrc are performed at T106 resolution. Due to the computational cost required, the high resolution simulations cover the shorter period 1979-1999.

At the beginning of each simulation, the soil has been set saturated with water and two years have been required in order to spin-up the soil moisture content. A simple analysis indicates that, in our models, two years were suitable to grant for the end of the transient behavior of the soil moisture content due to the abrupt initialization. After the first two years, no residual trend was present in the year to year variations of the soil moisture. Furthermore, a spin-up of two years has been considered enough in several previous studies (e.g: Ducharne et al., 1998; Knorr et al., 2001; Lu et al., 2005). The analysis that follows cover the period 1958-1999 for the coarse resolution simulations and the period 1981-1999 for the high resolution case.

3.2 Datasets used

The observed global monthly precipitation is obtained from the CMAP dataset (CPC Merged Analysis of Precipitation, Xie and Arkin, 1997) for the period 1979-1999. The land-only rainfall gauge-based dataset of the Climatic Research Unit (CRU; New et al., 2000) for the period 1958-1999 has been used as reference data for the continental-

only regions, because this allows to compare the model results for a longer time period. The surface albedo climatology is derived from the International Satellite Cloud Climatology Project (ISCCP) D1 monthly climatology (1984-1999). The ISCCP data were obtained from the NASA Langley Research Center Atmospheric Sciences Data Center. For the comparison of the model simulated vegetation leaf area index (LAI), the FASIR satellite derived LAI data have been used. The FASIR dataset covering the period 1982-1998 was obtained from the International Satellite Land Surface Climatology Project (ISLSCP) Initiative II dataset (Hall et al., 2005). ECMWF 40-year Re-Analysis (ERA40; more information about the ERA40 global analysis are available in http://www.ecmwf.int/research/era) have been used to derive the atmospheric fields of wind and specific humidity.

The surface latent and sensible heat fluxes from NCEP-DOE AMIP-II (henceforth NCEPII) reanalysis (Kanamitsu et al., 2002) for the period 1979-1999 is used for the comparison of the models simulated surface fluxes. It is important to note that reanalysis surface fluxes have to be carefully used for the validation of model simulations, as they are mostly derived from model physics and are, usually, not directly influenced by atmospheric assimilated observations (Kalnay et al., 1996). In this respect, NCEPII have been chosen as this reanalysis implements rainfall assimilation in the surface physics and improves the radiative transfer assimilation algorithms compared to previous NCEP reanalysis (Kalnay et al., 1996). Kanamitsu et al. (2002) showed that these improvements may also lead to better reanalysis surface fluxes.

The surface moisture flux has been computed from the latent heat flux from NCEPII by assuming a latent heat of vaporization of 28.935 $\frac{W \times day}{mm}$. In boreal summer this assumption is reasonable because the contribution from sublimation is negligible.

The vegetation distribution prescribed to EchOrc has been derived from the IGBP (International Geosphere Biosphere Programme) map at $1km \times 1km$ resolution and based on the Olson global ecosystems classification (Olson, 1994a,b).

4 Results

In this section the detailed evaluation of the model experiment results is shown. The robustness of the differences between the model simulations, and between model simulations and observations (or reanalyses) have been assessed by means of a t-test at the significance level of 5%.

In subsection 4.1, the vegetation seasonal cycle, as simulated by the EchOrc model, is evaluated. In subsection 4.2, we assess the major effects of the coupling of Echam4 with ORCHIDEE at T30 resolution whereas subsection 4.3 describes the sensitivity of the results to the numerical scheme used for the coupling and to the horizontal resolution. The results found for the Indian summer monsoon (ISM) region have been further discussed at the end of subsection 4.3.

4.1 Vegetation Leaf Area Index simulation

Figure 1 (panels a and c) shows the JFM (January-February-March) and JJA (June-July-August) LAI as simulated by EchOrc. A comparison with the satellite FASIR data (panel b and d) indicates that the simulated LAI is, in general, reasonably realistic. However, in several regions the amplitude of the seasonal variations is underestimated. The LAI seasonal cycle is particularly weak in semiarid tropical regions such as the Sahel, where the LAI is overestimated all year round.

In semiarid regions soil water deficit is the main environmental constraint for plant growth in the dry seasons. The weakness of the LAI seasonal cycle in these regions is a consequence of the way in which LAI is computed. In fact, as shown in section 2.3, the simulated LAI is a function of soil temperature only and the effect of the small soil moisture availability on plant growth is not accounted for in the present version of the model.

4.2 Summer surface climatologies

Figure 2 (panel a) shows the 2 meters temperature (T2m) as simulated by Echam4. Panels b and c show the fields as simulated by EchOrc and as it is found in the ERA40 data respectively, whereas in panel d the T2m difference between EchOrc and Echam4 is shown. Overall, due to the coupling of Echam4 with ORCHIDEE, a T2m increase is found in the continental regions of the northern hemisphere from middle to high latitudes, with the largest difference located over Eastern Asia (panel d). In the intertropical band a reduction of T2m is found over the Indian subcontinent, south America and over central and southern Africa.

Compared to ERA40 (see also section 4.3, figure 8 panels a and b), the T2m field simulated with the EchOrc model improves the cold bias found in Echam4 over eastern Asia. In particular the warmer T2m over eastern Siberia and Himalaya shown in the EchOrc simulations is in better agreement with the reanalysis. Also the reduced temperature over the Indian subcontinent, the Amazon basin and over the central and southern Africa appears to be closer to the observations. On the other hand, compared to ERA40, the increase in T2m simulated by EchOrc seems to be too high over extended areas of the northern continents (see figure 8, panels a and b). In particular EchOrc exhibits T2m higher than both ERA40 and Echam4 over central and western Asia, Middle East and central and Eastern United States, thus leading to a worse simulation in these regions.

Four areas of the globe with strong effects on the Echam4 simulated climate will be analyzed with greater detail in the following. The four selected areas are the Indian summer monsoon (ISM), the Amazon basin, the central Africa (hereinafter Africa) and the Eurasia region. These four regions are covered with vegetation: tropical forests and rainforests are found over Amazon basin and Africa, boreal forest cover the Eurasia and agriculture mixed to forest extends over the ISM region. The analyzed surface variables averaged over these regions are presented in Tables 2-4.

In table 2 the JJA mean values of roughness length (Z0) and albedo as simulated by Echam4 and EchOrc are reported, along with the satellite albedo from ISCCP D1 monthly

climatology. The results shown in table 2 suggest that some contribution to the temperature decrease over the Indian subcontinent and over central Africa could be due to the surface albedo increase found in the EchOrc simulations. Changes are found also in the roughness length, especially over the Amazon basin.

Figure 3 (panels a-c) shows the surface latent heat flux (LHF) as simulated by Echam4, EchOrc and in the NCEPII reanalysis data, respectively. Panel d shows the differences between EchOrc and Echam4. In the EchOrc ensemble mean there is a systematic increase of LHF over vegetated areas. This is in agreement with the reanalysis, in particular over boreal and tropical forests (see also section 4.3, figure 10 panels a and b). In the Sahel region (10-20°N, 10°W-20°E) the simulated LHF is too strong in Echam4 and the bias is even more pronounced in the EchOrc simulations. This bias might be explained by the fact that, in that region, EchOrc shows an overestimation of the LAI and, as a consequence, of the simulated fraction covered with vegetation (see section 2.3). Since the albedo over vegetated areas is lower than over bare soil in dry regions such as the Sahel, it follows a decrease in surface albedo with respect to the Echam4 simulations (25% reduction averaged over the region used to define the Sahel Rainfall Index in Moron et al., 2003). The increase of precipitation and of the subsequent evapotranspiration is a consequence of the reduced albedo, in agreement with the Charney's albedo mechanism of self induction of deserts (Charney et al., 1977).

The increased LHF in vegetated areas found in the EchOrc simulations is, in most regions, compensated by a decrease of sensible heat flux (not shown), which results in a considerable reduction of the Bowen ratio during boreal summer. Table 3 contains the Bowen ratio averaged over the four selected areas. The systematic decrease found in the EchOrc simulations is in better agreement with the reanalysis, with the only exception of Eurasia. In fact, the anomalously low evaporation rate found for Echam4 in that region is not compensated by an increase in sensible heat flux. This means that, less energy is available at the surface due to reduced net surface radiation or energy loss resulting from the coupling numerical scheme (see section 4.3).

Figure 3 (panels e and f) shows the percentage of evapotranspiration due respectively to transpiration and to interception loss as simulated by EchOrc. No corresponding quantity are available for the Echam4 simulations, as those processes are not explicitly considered in the land surface scheme included in this model (see section 2). The comparison of panel f with panel d suggests that the interception loss contribution in vegetation covered areas is, at least in part, responsible of the increase in surface evapotranspiration.

Figure 4 shows the total precipitation. Compared to Echam4 (panel a), EchOrc (panel b) exhibits increased precipitation over boreal forests, Amazon basin and central Africa tropical forests (panel d). Interestingly, precipitation over the Asian monsoon region is substantially increased, leading to a significant improvement of the simulated monsoon. As mentioned earlier, in the EchOrc simulations increased precipitation is found in the Sahel region, producing a worse simulation of the rainfall in that region. As shown in figure 4, EchOrc simulates higher summer precipitation compared to both Echam4 and CMAP data over wide areas of the continents north of 45 degrees (see also figure 11, panels a and b). This results might indicate a worsening of the simulated precipitation over these areas with EchOrc. However, it should be noted that some uncertainty is associated with CMAP precipitation data at middle and high latitudes. As pointed out by Xie and Arkin (1995, 1997), no observation-based data sources provide coverage with reasonable quality over these regions. Furthermore, as stated by Legates and Willmott (1990), most of the standard raingauge measurements, used in order to produce the global precipitation datasets, such as CMAP, underestimate the actual precipitation. The raingauge undercatch tends to increase as the latitude increases and it can range from less than 5% in the tropics to more than 40% at the geographical poles (Legates and Willmott, 1990; Hagemann and Dümenil, 1998). The high uncertainty associated with the precipitation observations at middle and high latitudes over continental areas is demonstrated by comparing the CMAP boreal summer climatology with the independently compiled CRU continents only dataset (New et al., 2000). The boreal summer climatologies have been computed for the period 1979-1999 for both CMAP and CRU. In the tropics the two datasets are very

close to each other (when averaged over the 20°S-20°N latitude band CRU displays a 2% decrease compared to CMAP). At higher latitudes (45-90°N), the CRU dataset displays an area averaged increase in precipitation of more than 15% compared to CMAP, with the strongest increase over Greenland and Asia (not shown). Compared with the CRU data, the results obtained at high latitude with EchOrc and Echam4 appear to be quite different (not shown). Echam4, in fact, appears to underestimate the precipitation over most of the northern Eurasia while EchOrc looks considerably better in middle and high latitudes of the northern continents.

As shown in Table 3, the increased precipitation, found in EchOrc, produces an increase of the soil wetness in the ISM and Eurasia regions. On the other hand, decreases of soil wetness are found over the Amazon basin and the Africa regions, despite of the higher precipitation. In the Amazon basin, the reduction of soil moisture is closely tied to the smaller accumulation of rainfall during the previous months, while in Africa, both the reduced rainfall accumulation and the subsequent increased E-P found in EchOrc in boreal summer (See Table 4) contributes to reduce the simulated soil wetness.

Table 4 describes the hydroclimatology, in the four selected regions, for the model simulations at T30 and at T106 resolution as well as for the observations. The model results at high horizontal resolution will be discussed in section 4.3. In Table 4 the boreal summer climatological mean precipitation ($\bar{P}$), evapotranspiration ($\bar{E}$) and moisture convergence ($-divQ$) averaged over each region are reported. Moisture convergence has been evaluated using the balance equation for the total water substance in the atmosphere. Following Peixoto and Oort (1992), we can simplify the general balance equation after averaging in time and in space over a region bounded by a conceptual vertical wall as follows:

$$\left\{\frac{\overline{\triangle W}}{\triangle t}\right\} + \{div\bar{Q}\} = \{\bar{E} - \bar{P}\} \tag{9}$$

where the overbar indicates the time and the braces stand for the space average, respectively. $\bar{Q}$ is the vertically integrated horizontal transport of water vapor from the Earth's surface to the top of the atmosphere. $\bar{W}$ is the amount of water vapor contained in a unit area atmospheric column of air. ERA40 data have been used in order to evaluate $\bar{W}$ for

the computation of $\left\{div\bar{Q}\right\}$ in the observation/reanalysis case. It should be noted that the datasets used for the computation of $\left\{div\bar{Q}\right\}$ in the reanalysis/observation case may not be completely consistent each other because of biases in the reanalysis data.

Table 4 shows that, in the four regions considered, both precipitation and evapotranspiration considerably increase in the EchOrc simulations. This is in general agreement with the observations except for the Eurasia region where the increased simulated precipitation is too strong. In this region both the models show small positive convergence values, in contrast with the observation/reanalysis case which exhibits large negative values. The intense moisture convergence simulated by EchOrc might explain the excess of precipitation. Looking at the moisture convergence, we can note that the convergence values are lower in the EchOrc simulations than in those performed with Echam4, with the exception of the ISM case. This suggests that the increase of precipitation could be due to an increased moisture supply from the surface. The same suggestion applies also to the ISM region, as the EchOrc simulated increase of precipitation, in that region, is about two times the increase of moisture convergence.

In figure 5 (panels a-c) the 850mb global wind field as simulated by Echam4, by EchOrc and as in the ERA40 data is shown. The difference between the EchOrc and the Echam4 simulations (panel d) shows a rather strong impact of the coupling with ORCHIDEE on the Echam4 circulation. The stronger effect is found over the northern hemisphere continents, Africa and northern South America. Improvements in the simulated 850mb wind field are found over the north-west China desert, Mongolia and Tibet, with an increase of the southward flow toward the Tibetan Plateau. A significant improvement is also found in the circulation over the Indian Ocean, and in particular over the ISM region as it will be discussed in section 4.3.3.

The westerly flow over eastern Africa, north of the Equator, is stronger in EchOrc than in Echam4. This tends to increase the model bias and , probably, it is partly due to the decrease in surface roughness length in that region (not shown).

At the beginning of this section, it was shown that in the EchOrc simulations there is

an increase of the T2m over northern hemisphere continental regions (Figure 2). As a consequence, a reduction in the sea level pressure (SLP) field (not shown) is found over large areas of Asia and North America. This leads to an enhancement of the SLP sea-land contrast which affects the atmospheric circulation also over oceans. In particular, the anticyclonic flow over the tropical Atlantic is enhanced in the EchOrc model due to the intensification of the high pressure centers in that region. It follows a modification of the circulation over the Gulf of Mexico, Caribbean Sea and North American basin where precipitation is reduced producing patterns more similar to the observations (see figure 4). The increased anticyclonic activity in this region is also related to the effects on the local meridional circulation (not shown) associated with the increased convection activity over the Amazon basin.

4.3 Sensitivity to horizontal resolution

4.3.1 Numerical scheme effects

In section 4.2, increased surface air temperature was found in extended mid-to-high latitude continent areas of northern hemisphere, as a consequence of the coupling of Echam4 with ORCHIDEE. From June to August, continental regions, such as eastern Asia, exhibit a strong rate of change in surface temperature and are, as a consequence, affected by energy loss at the surface-atmosphere interface due to the semi-implicit coupling numerical scheme (Schulz et al., 1998) in the simulations performed with Echam4. In fact, in Echam4, due to the semi-implicit coupling scheme used, the surface energy balance equation is solved after that the radiation scheme has computed the radiation transfer through the atmosphere, and after that the vertical diffusion scheme has calculated the fluxes exchanged with the lower layers of the atmosphere. This means that the fluxes balanced by the surface energy equation are different from those actually received by the lower atmosphere. In contrast, the implicit method used in the coupling with ORCHIDEE conserves the energy because the surface fluxes and the surface energy balance are computed simultaneously (Polcher et al., 1998).

Figure 6 (panel a) shows the JJA mean residual surface heat budget, that is the difference between the energy flux toward the atmosphere, as computed in the surface energy balance, and the flux actually given to the atmosphere in the Echam4-T30 simulations. As it is clear from the figure, a very high energy imbalance is found in regions where high surface temperature increments are encountered during boreal summer. The stronger energy loss is located over the Himalaya and in the continental East-Asia. The surface energy imbalance described is a consequence of using a semi-implicit coupling between surface and atmosphere, whose impact on the simulation of the mean climate depends on the time step of integration of the model. Figure 6 (panel c) shows the boreal summer residual surface heat budget for the Echam4 simulation performed at higher resolution (T106). In the Echam4-T106 simulations, the energy imbalance, even if present, is reduced to very small values. The surface physics used at T106 is exactly the same used at coarser resolution and the only change is the reduction of the time step of integration from 1800 sec to 720 sec. It follows that the shorter time step is responsible of the strongly reduced residual surface heat budget.

To give further evidence of the role of the time step on the surface energy loss, an experiment has been performed, for the period 1979-1999, using Echam4 at T30 resolution but with the same time step which is normally used in a T106 integration (hereinafter Ech4-T30 ($\Delta t = 720s$) experiment). It's worth noting here that, as suggested by Stendel and Roeckner (1998), every change in the time step of integration as well as in the horizontal resolution, should be followed by a tuning of the parameters related to the processes subject to some time scale dependencies (e.g.: horizontal diffusion, the precipitation formation efficiency and, hence, cloud lifetime). This kind of tuning would be necessary in order to keep the model climatologies close to observations (Stendel and Roeckner , 1998). As the exclusive objective was the assessment of the effect of the shorter integration time step on the surface energy imbalance due to the numerical scheme, the Ech4-T30 ($\Delta t = 720s$) experiment has been set up without any tuning of the "scale-sensitive" parameters.

The JJA mean residual surface heat budget obtained from the Ech4-T30 ($\Delta t = 720s$) experiment is shown in figure 6 (panel b). Interestingly, the energy loss at the interface, in this experiment, is reduced at the low values found for the T106 resolution case (see figure 6, panel c). Furthermore, as shown in figure 7, the surface energy imbalance turns out to be a major factor for continental East-Asia and North America difference in simulated surface air temperature between low (panel a) and high resolution (panel c) Echam4 versions. These results indicate that the numerics of the model, and in particular the use of a semi-implicit or fully implicit coupling scheme, may play an important role in the surface energy budget and in the surface air temperature simulation. Interestingly, the T2m difference between Echam4-T30 and Ech4-T30 ($\Delta t = 720s$), in figure 7 (panel d), closely resembles the T2m difference obtained comparing Echam4 with EchOrc (figure 2, panel d). This indicates that the surface energy loss at the surface-atmosphere interface, found in Echam4, might explain at least part of the differences in the simulated T2m field between Echam4 and EchOrc at coarse resolution.

4.3.2 Comparison of the results at different horizontal resolution

This section aim to study in detail the sensitivity of the T30 simulation results, presented in section 4.2, to the increased horizontal resolution. Four pictures are presented, each of which is organized as follows: each figure contains 4 panels, showing the differences between the simulated fields (at T30 and at T106, and with and without the ORCHIDEE LSM) and observation/reanalysis. In order to make it simpler to verify whether the changes obtained with the new LSM produce results closer to the observations, only the grid-points with significant differences (exceeding the 5% significance level) between EchOrc and Echam4 are displayed. Panels a and c represent the differences of the Echam4 field with respect to observations/reanalyses and panels b and d display the corresponding EchOrc differences. Upper panels correspond to T30 resolution simulations and lower panels to T106 simulations.

Figure 8 shows the difference in T2m between the model simulations and ERA40.

Compared to the T30 (panels a and b), the T106 simulations (panels c and d) exhibit a considerable reduction of the biases with respect to reanalysis. Furthermore, comparing panel a with panel c and panel b with panel d, respectively, it is shown that, at T106, in middle and high latitude regions, the differences between Echam4 and EchOrc biases become much smaller than at T30 resolution. As explained in the previous section, this follows, at least in part, from the reduced surface energy imbalance due to the semi-implicit coupling numerical scheme at higher resolution. Differently from the middle and high latitude case, in tropical regions, the T2m differences between Echam4 and EchOrc T106 simulations are similar to those observed in the T30 case. In fact, in agreement with the reanalysis, a decrease in T2m over the Indian subcontinent, the Amazon basin and central and southern Africa is found in EchOrc also at T106.

Figure 9 shows the differences in the wind field at 850 mb between the model simulations and reanalysis. The results of the T106 case (panels c and d) compared with those at coarser resolution (panels a and b) show a considerable reduction of the bias with respect to reanalysis, reflecting the better representation of the atmospheric dynamics at higher horizontal resolution (Stendel and Roeckner , 1998). Furthermore, figure 9 shows that the difference in the wind field induced by the coupling between Echam4 and ORCHIDEE is considerably reduced at higher resolution, in particular in middle and high latitudes of the northern hemisphere. Probably, in many regions, this is the consequence of the reduced energy loss at the surface-atmosphere interface (see figure 6) due to the semi-implicit coupling (see section 4.3) in Echam4 at T106. In fact the northern hemisphere SLP difference, between Echam4 and EchOrc, found at T30 (see section 4.2) mostly disappear at T106 (not shown). In the T106 resolution case, even if of minor extent, the differences on the 850 mb atmospheric circulation induced by the coupling between Echam4 and ORCHIDEE over Indian Ocean, central eastern Africa and ISM region are of the same sign as in the T30 case. In particular, the Somali jet strength is enhanced and so the intensity of the Indian Summer monsoon, in agreement with the reanalysis data.

Figure 10 compares the models LHF with the reanalysis data. LHF differences between

Echam4 and EchOrc show a very weak sensitivity to the change in horizontal resolution. This is also visible from Table 4, where the evapotranspiration ($\bar{E}$) values averaged over the different regions show, for each model, very small changes between T30 and T106 simulations. A considerable exception is found in the Eurasia region, where, in Echam4, $\bar{E}$ increases by $\sim$20% passing from low to high resolution. Interestingly, this is also the only region with a significant increase in the Bowen ratio in Echam4 (not shown), reflecting the fact that there is an increase of surface energy available because of a reduced energy loss caused by the numerical coupling scheme at higher resolution (See figure 6).

Figure 11 shows the differences in total precipitation between simulations and observations. From these results it appears evident a considerable reduction of the biases with respect to observations in the high resolution case in EchOrc as well as in the Echam4 simulations. Despite of the reduced bias, the results of the T106 simulations show increase in precipitation over vegetation covered areas in EchOrc, in particular over tropical and boreal forests, similarly to the T30 case. In Table 4 it is shown that the increase in precipitation, over the four regions considered, found in the EchOrc simulations at coarse resolution are essentially the same at T106. Furthermore, the convergence ($-divQ$) terms become closer to each other between Echam4 and EchOrc, at higher resolution, reflecting less impact due to the coupling with ORCHIDEE in the Echam4 atmospheric circulation (See figure 9).

In the Sahel region, the increase in precipitation due to the coupling of Echam4 with ORCHIDEE found at T106 (figure 11, panels c and d) leads to an increase of the bias in that region and is similar to that found at T30 resolution (figure 11, panels a and b; see also figure 4). As discussed in section 4.2, this increase is consistent with the Charney's albedo mechanism of self induction of deserts. In fact, the bias in the simulated fraction covered with vegetation is responsible of a decrease in surface albedo with respect to Echam4 (a 22% decrease is found in this case; the value has been computed as described in section 4.2), thus leading to increased precipitation and evapotranspiration (Charney et al., 1977).

4.3.3 Indian Summer Monsoon region

Figure 12 shows the differences in precipitation (panels a and b), LHF (panels c and d) and T2m (panels e and f) between the model simulations at T30 resolution and reanalysis/observations over the South-East Asian monsoon region. Only the grid-points with significant differences (exceeding the 5% significance level) between EchOrc and Echam4 are displayed. The left panels refer to the Echam4 model and the right ones to the EchOrc simulations. Figure 13 shows the same panels as in figure 12 but for the simulations at T106 resolution.

The comparison between figure 12 and figure 13 shows that very robust impacts are found in the south-east Asian summer monsoon region, despite of the change of the horizontal resolution. Furthermore, all the surface fields considered appear to be better simulated with the EchOrc model at coarse as at high resolution. It is noteworthy that, in the T106 resolution case similar improvements are found in the precipitation pattern over the Bay of Bengal and in the Indian subcontinent thanks to the coupling with ORCHIDEE, even if the impacts on the atmospheric circulation are minor than in the T30 resolution case (See figure 9).

As pointed out in the previous section, the increase in the JJA precipitation found in the EchOrc simulations in the ISM continental regions could be partially due to the increase in the water recycling from the surface. From Table 4 it is shown that nearly half of the increase in atmospheric precipitable water availability is accounted for, in the climatological average, by surface moisture recycling in the T30 simulations, while in the T106 case it is close to 2/3. The remaining part of the increase described is linked to the moisture convergence. The reduced contribution due to convergence found at higher resolution reflects the fact that in this case there are fewer impacts on the atmospheric circulation. The behavior described above is consistent with the monsoon land-atmosphere feedback mechanism proposed by Lau and Bua (1998) who argued that the increase in evaporation is able to further moisten and destabilize the atmospheric boundary layer triggering the rapid growth of deep convection and precipitation. The tropospheric air so warmed

further rises, leading also to increased low level moisture convergence.

Figure 14 shows the climatological seasonal cycles of precipitation (panels b and g), T2m (panels c and h), surface moisture flux (panels d and i), and atmospheric moisture convergence (panels e and l; moisture convergence is computed as explained in section 4.2) averaged over the ISM region (continents only points), as simulated by the models and in the reanalysis/observations. Left panels represent T30 resolution simulations while right panels show T106 resolution results. Panels a and f display also the IMI index, defined by Wang et al. (2001) as the difference of the summer mean zonal wind at 850 mb averaged over 40-80E, 5-15N and the same field averaged over 70-90E, 20-30N. This dynamic index is generally considered a good indicator of the strength of the Indian monsoon in the observations as well as in the Echam4 AGCM (Cherchi and Navarra, 2005). The EchOrc model simulates in a more realistic way the seasonal cycle over the ISM region for all the variables, at low as at high resolution. In particular, in the early stage (June) there is a stronger monsoon (panels a and f) in the simulations with EchOrc in agreement with the reanalysis/observations. In the onset phase of the monsoon the increased surface moisture flux, compared to the Echam4 simulations, seems to trigger the intensity of the monsoon circulation, in the EchOrc model, leading also to increased convergence (panels e and l). The final effect is an increased precipitation (panels b and g) expecially in June but also in the subsequent months. The better simulations of surface latent heat flux and of the cloud cover (not shown; the cloud cover is increased according to the stronger precipitation) lead also to a better representation of the surface air temperature during the summer months (panels c and h).

5 Conclusions

In this study we have coupled the Echam4 AGCM with an early version of the ORCHIDEE LSM. The results indicate that the Echam4-ORCHIDEE (EchOrc) coupled model is able to simulate reasonably well the boreal summer vegetation Leaf Area Index (LAI). However, in many semiarid regions such as the Sahel, the amplitude of the LAI seasonal

variations is underestimated. This is a consequence of the way in which LAI is computed in the model, as it does not consider the effect of the small soil moisture availability, during the dry seasons, on the vegetation leaf growth.

Strong impacts are found on the boreal summer surface climate of the Echam4 AGCM due to the coupling with ORCHIDEE. A systematic precipitation increase is found over vegetation covered areas. In particular, the enhanced precipitation, in the EchOrc model, over the Amazon basin, central Africa and ISM region is in agreement with the observations. The increased precipitation is accompanied by an enhancement in the evapotranspiration from the surface, and this is at least in part due to the interception loss contribution coming from the vegetation canopies.

The coupling with ORCHIDEE has been shown to have a considerable impact on the boreal summer surface air temperature simulated by Echam4. A warmer 2 meters temperature (T2m) is found over large continental areas in middle and high latitudes of the northern hemisphere. A particularly strong T2m increase is found over Eastern Asia. The warmer temperature over these areas also leads to increased land-sea contrast in sea level pressure (SLP), which, in turn, induces changes in the atmospheric circulation.

Effects on the atmospheric circulation are found over northern hemisphere continents, Africa and northern South America, but also over oceans. In particular, over tropical Atlantic the anticyclonic flow is enhanced in the EchOrc model. A significant improvement of the circulation is found also over the tropical Indian Ocean.

The implicit numerical scheme implemented in order to couple ORCHIDEE with Echam4 has been shown to have a considerable impact on the surface energy budget of extended continent areas of the northern hemisphere. In particular, in these regions, it has been shown that the surface energy imbalance due to the semi-implicit coupling is a major factor for the explanation of the differences in the simulated T2m field between Echam4 and EchOrc at coarse resolution. Furthermore, the energy loss at the surface, owing to the numerical scheme implemented in Echam4, has been found to depend on the model integration time step, so that a shorter time step reduces the energy imbalance at the

surface-atmosphere interface.

The impacts on the T2m and on the atmospheric circulation fields have shown some sensitivity to the increase in horizontal resolution. These fields simulated by Echam4 and EchOrc at T106 resolution become much closer to each other than at T30 resolution, reflecting in part the fact that the effect of the coupling numerical scheme mostly disappears at higher resolution. Furthermore, the comparison of the T106 simulations with those at lower resolution shows a considerable reduction of the biases with respect to observations/reanalysis, as a consequence of the better representation of the atmospheric dynamics in the models at higher horizontal resolution (Stendel and Roeckner , 1998).

The effects found on the precipitation and on the evapotranspiration fields due to the coupling of Echam4 with ORCHIDEE are robust despite of the change in horizontal resolution. Four vegetated regions have been chosen on the basis of the particular interest and because of the strong impact of the improved representation of land-surface and vegetation processes. The four regions are the Indian Summer Monsoon (ISM), the Amazon basin, the central Africa and the Eurasia region. The increase in precipitation over all these four regions found in the EchOrc simulations is essentially the same at coarse as well as at high resolution. The atmospheric moisture convergence values in all the regions, except for ISM, are lower in EchOrc than in Echam4. This suggests that, in these regions, the increase in precipitation is due to the enhanced atmospheric precipitable water supply from the surface. Instead, in the ISM region, the increase in precipitation might follow from both increased moisture flux from the surface and enhanced moisture convergence.

The EchOrc model simulates in a more realistic way the spatial pattern and the seasonal cycle of the climatological surface fields and fluxes as well as the atmospheric moisture convergence in the ISM region. In particular, in its early stage (June), the monsoon intensity is stronger, in agreement with the reanalysis/observations. In the onset phase of the monsoon, the increased moisture flux from the surface, compared to the Echam4 simulations, seems to trigger the intensity of the monsoon circulation in the EchOrc model, leading also to increased moisture convergence. The final effect is an increased precip-

itation expecially in June but also in the subsequent months. This kind of behavior is consistent with the monsoon land-atmosphere feedback mechanism proposed by Lau and Bua (1998).

Land surface-vegetation processes have considerable bio-physical effects on climate and, as evidenced in this study, their inclusion in AGCMs is a major task in order to improve our skill in surface climate simulation. In this work, a prescribed vegetation representation has been used and the seasonal cycle of the vegetation cover is simply computed as a function of soil temperature. From this kind of approach, it follows an unrealistically small vegetation cover interannual variability and, as shown in this work, a poor representation of the seasonal cycle in semiarid tropical regions. In particular, this latter shortcoming has been shown to contribute to the precipitation bias found in EchOrc over the Sahel. By virtue of these considerations, a further improvement in the simulated surface climate is expected from the inclusion in the EchOrc AGCM of a fully interactive dynamical global vegetation model, which is suitable to reproduce in a more realistic way the interannual and seasonal variations in the vegetation characteristics.

Acknowledgements. The authors thank the ITALY-USA Cooperation Program in Climate Science and Technology and the European Community project ENSEMBLES (contract GOCE-CT-2003-505539) for the financial support. The experiments used for this study has been executed on the NEC SX-6 at INGV in Bologna, and authors are grateful to L.Amato, A.Cherchi, L. Giacomelli, E. Manzini, E. Scoccimarro and M. Vichi for usefull discussions and for the technical support given.

References

Barros, A.P., and H. Wenje, 2002: A study of land-atmosphere interactions during summertime rainfall using a mesoscale model; *J. Geophys. Res.*, **107(D14)**, 4227.

Bonan, G., 2002: *Ecological Climatology*; Cambridge University Press, Cambridge, 678 pp.

Chalita, S., and H. LeTreut, 1994: The albedo of temperate and boreal forest and the northern hemisphere climate: a sensitivity experiment using the LMD GCM; *Clim. Dyn.*, **10(4-5)**, 231–240.

Charney, J., 1975: Dynamics of deserts and drought in the Sahel; *Quart. J. Roy. Meteor. Soc.*, **101**, 193–202.

Charney, J., W.J. Quirk, S.-H. Chow, and J. Kornfield, 1977: A comparative study of the effects of albedo change on drought in semi-arid regions; *J. Atm. Sci.*, **34**, 1366–1385.

Cherchi, A., and A. Navarra: Sensitivity of the Asian summer monsoon to the horizontal resolution: Differences between AMIP-type and coupled model experiments. Submitted to Clim Dyn.

Cherchi, A., and A. Navarra, 2003: Reproducibility and predictability of the Asian summer monsoon in the Echam4-GCM; *Clim. Dyn.*, **20**, 365–379.

de Rosnay, P., and J. Polcher, 1998: Modeling root water uptake in a complex land surface scheme coupled to a GCM; *Hydrology and Earth System Sciences*, **2(2-3)**, 239–256.

Dirmeyer, P.A., and J. Shukla, 1994: Albedo as a modulator of climate response to tropical deforestation; *J. Geophys. Res.*, **99**, 863–877.

Ducharne, A., K. Laval, and J. Polcher, 1998: Sensitivity of the hydrological cycle to the parameterization of soil hydrology in a GCM; *Clim. Dyn.*, **14**, 307–327.

Ducoudré, N., K. Laval, and A. Perrier, 1993: SECHIBA, a New Set of Parameterizations of the Hydrologic Exchanges of the Land-Atmosphere Interface within the LMD Atmospheric General Circulation Model; *J. Climate*, **6**, 248–273.

Hagemann, S., and L. Dümenil, 1998: A parameterization of the lateral waterflow for the global scale; *Clim. Dyn.*, **14**, 17–31.

Hall, F., G. Collatz, S. Los, E. Brown de Colstoun, and D. Landis, *eds. ISLSCP Initiative II. NASA. DVD/CD-ROM* NASA, 2005.

Henderson-Sellers, A., R.E. Dickinson, T.B. Durbidge, P.J Kennedy, K. McGuffie and A.J. Pitman, 1993: Tropical deforestation: Modeling local- to regional-scale climate change; *J. Geophys. Res.*, **98(D4)**, 7289–7315.

Kalnay, E., M. Kanamitsu, R. Kistler, W. Collins, D. Deaven, L. Gandin, M. Iredell, S. Saha, G. White, J. Woollen, Y. Zhu, A. Leetmaa, M. Chelliah, W. Ebisuzaki, W. Higgins, J. Janowiak, K.C. Mo, C. Ropelewski, J. Wang, R. Jenne, and D. Joseph, 1996: The NCEP/NCAR 40-Year Reanalysis Project; *Bull. Amer. Meteor. Soc*, **77 (3)**, 437-471.

Kaufmann, R.K., R.B. Myneri, C.J. Tucker, D. Slayback, N.V. Shabanov, and J. Pinzon, 2003: The effect of vegetation on surface temperature: A statistical analysis of NDVI and climate data; *Geophys. Res. Lett.*, **30**, 2147, doi:10.1029/2003GL018251.

Kittredge, J., 1948: *Forest Influences: The Effects of Woody Vegetation on Climate, Water, and Soil, with Applications to the Conservation of Water and the Control of Floods and Erosion*; McGraw-Hill, New York.

Koster, R. D., P. A. Dirmeyer, A. N. Hahmann, R. Ijpelaar, L. Tyahla, P. Cox, and M. J. Suarez, 2002: Comparing the degree of land-atmosphere interaction in four atmospheric general circulation models; *J. Hydrometeor.*, **3**, 363–375.

Koster, R. D., M. J. Suarez, R. W. Higgins, and H.M. Van den Doll, 2003: Observational evidence that soil moisture variations affect precipitation; *Geophys. Res. Lett.*, **30(5)**, 1241, doi:10.1029/2002GL016571.

Koster, R. D., and M. J. Suarez, 2004: Suggestion in the Observational Record of Land-Atmosphere Feedback Operating at Seasonal Time Scales; *J. Hydrometeor.*, **5(3)**, 567–572.

Koster, R. D., P. A. Dirmeyer, Z. Guo, G. Bonan, E. Chan, P. Cox, C. T. Gordon, S. Kanae, E. Kowalczyk, D. Lawrence,P. Liu,C. Lu,S. Malyshev,B. McAvaney,K. Mitchell,D. Mocko,T. Oki,K. Oleson, A. Pitman,Y. C. Sud,C. M. Taylor,D. Verseghy,R. Vasic,Y. Xue, and T. Yamada, 2004: Regions of Strong Coupling Between Soil Moisture and Precipitation; *Science*, **305**, 1138–1140.

Krinner, G., N. Viovy, N. de Noblet-Ducoudre, J. Ogee, J. Polcher, P. Friedlingstein, P. Ciais, S. Sitch, and I.C. Prentice, 2005: A dynamic global vegetation model for studies of the coupled atmosphere-biosphere system; *Global Biogeochem. Cy.*, **19(1)**, Art.No. GB1015.

Kanamitsu, M., W. Ebisuzaki, J. Woollen, S.-K. Yang, J.J. Hnilo, M. Fiorino, and G.L. Potter, 2002: NCEP-DOE AMIP-II Reanalysis (R-2); *Bull. Amer. Meteor. Soc*, **83 (11)**, 1631-1643.

Knorr, W., K.G. Schnitzler, and Y. Govaerts, 2001: The role of bright desert regions in shaping North African climate; *Geophys. Res. Lett.*, **28(18)**, 3489–3492.

Knorr, W., and K.G. Schnitzler, 2006: Enhanced albedo feedback in North Africa from possible combined vegetation and soil-formation processes; *Clim. Dyn.*, **26**, 55–63.

Lau, K.-M., and W. Bua, 1998: Mechanisms of monsoon-Southern Oscillation coupling: Insights from GCM experiments; *Clim. Dyn.*, **14**, 759–779.

Lawrence, D.M., and J.M. Slingo, 2004: An Annual Cycle of Vegetation in a GCM. Part II: Global Impacts on Climate and Hydrology; *Clim. Dyn.*, **22(2-3)**, 107–122.

Legates, D.R., and C.J. Willmott, 1990: Mean Seasonal and Spatial Variability in Gauge-Corrected, Global Precipitation; *Int. J. Climatology*, **10**, 111–127.

Lu, C.H., M. Kanamitsu, J.O. Roads, W. Ebisuzaki, K.E. Mitchell, and D. Lohmann, 2005: Evaluation of soil moisture in the NCEP-NCAR and NCEP-DOE global reanalyses; *J. Hydrometeor.*, **6(4)**, 391–408.

Manabe, S., 1969: Climate and the ocean circulation I. The atmospheric circulation and the hydrology of the earth's surface; *Mon. Wea. Rev.*, **97**, 739–774.

McGuffie, K., A. Henderson Sellers, H. Zhang, T.B. Durbridge, and A.J. Pitman, 1995: Global climate sensitivity to tropical deforestation; *Global and Planet change*, **10(1-4)**, 97–128.

Meehl, G.A., and W.M. Washington, 1988: A comparison of soil moisture sensitivity in two global climate models; *J. Atm. Sci.*, **45**, 1476–1496.

Moron, V., N. Philippon, and B. Fontaine, 2003: Skill of Sahel rainfall variability in four atmospheric GCMs forced by prescribed SST; *Geophys. Res. Lett.*, **30(23)**, Art.No. 2221.

New, M., M. Hulme, and P. Jones, 2000: Representing Twentieth-century space-time climate variability. Part II: development of 1901-1996 monthly grids of terrestrial surface climate; *J.*

Climate, **13**, 2217–2238.

Peixoto, J.P., and A.H. Oort, 1992: *Physics of climate*; American Institute of Physics (AIP), New York.

Olson, J.S., 1994a: Global ecosystem framework-definitions; *USGS EROS Data Center International Report*, Sioux Falls, SD, 37 pp.

Olson, J.S., 1994b: Global ecosystem framework-translation strategy; *USGS EROS Data Center International Report*, Sioux Falls, SD, 39 pp.

Patterson, K.A., 1990: Global distributions of total and total-available soil water-holding capacities; *M.S. Thesis*, Dept. of Geography, University of Delaware, 199 pp.

Polcher, J., B. McAvaney, P. Viterbo, M.A. Gaertner, A. Hahmann, J.F. Mahfouf, J. Noilhan, T. Philipps, A. Pitman, C.A. Schlosser, J.P. Schulz, B. Timbal, D. Verseghy, Y. Xue, 1998: A proposal for a general interface between land surface schemes and general circulation models; *Glob. Plan. Change*, **19(1-4)**, 261–276.

Polcher, J., 1994: Etude de la sensibilité du climat tropicale à la deforestation; *PhD Thesis*, Université Pierre et Marie Curie, Paris VI 185 pp.

Polcher, J., and K. Laval, 1994: A statistical study of the regional impact of deforestation on climate in the LMD GCM; *Clim. Dyn.*, **10**, 209–219.

Rayner, N.A., D.E. Parker, E.B. Horton, C.K. Folland, L.V. Alexander and P. Frich, 2000: The HadISST1 Global Sea-Ice and Sea Surface Temperature Dataset, 1871–1999; *Hadley Center Technical Note 17*.

Roeckner, E., K. Arpe, L. Bengtsson, S. Brinkop, L. Dümenil, M. Esch, E. Kirk, F. Lunkeit, M. Ponater, B. Rockel, R. Sausen, U. Schlese, S. Schubert, and M. Windelband, 1992: Simulation of the present-day climate with the ECHAM model: impact of model physics and resolution *Max-Planck Institut für Meteorologie*, Report no. 93, Hamburg, 172 pp.

Roeckner, E., K. Arpe, L. Bengtsson, M. Christoph, M. Claussen, L. Dümenil, M. Esch, M. Giorgetta, U. Schlese and U. Schulzweida, 1996: The Atmospheric general circulation Model ECHAM4: Model description and simulation of present-day climate: *Max-Planck Institut für Meteorologie*, Report no. 218, Hamburg, 86 pp.

Shukla, J., and Y. Mintz, 1982: Influence of land-surface evapotranspiration and the Earth's climate; *Science*, **219**, 1498–1501.

Schulz, J.P., L. Dümenil, J. Polcher, C.A. Schlosser, and Y. Xue, 1998: Land surface energy and moisture fluxes: comparing three models; *J. Appl. Meteor.*, **37**, 288–307.

Schulz, J.P., L. Dümenil, and J. Polcher, 2000: On the land-surface/atmosphere coupling and its impact in a single column atmospheric model; *J. Appl. Meteor.*, **40**, 642–663.

Schubert S.D., M.J. Suarez, P.J. Pegion, R.D. Koster, and J.T. Bacmeister, 2004: On the Cause of the 1930s Dust Bowl; *Science*, **303**, 1855–1859.

Stendel, M., and E. Roeckner, 1998: Impacts of horizontal resolution on simulated climate statistics in ECHAM-4; *Max-Planck Institut für Meteorologie*, Report no. 253, Hamburg, 57 pp.

Stewart, J.B., 1977: Evaporation from the wet canopy of a pine forest; *Water Resources Research*, **13**, 915–921.

Stull, R.B., 1997: *An introduction to Boundary Layer Meteorology*; Kluwer Academic, Dordrecht, 670 pp.

Sud, Y.C., J. Shukla, and Y. Mintz, 1988: Influence of land surface roughness on atmospheric circulation and precipitation: a sensitivity study with a general circulation model; *J. Appl. Meteor.*, **27**, 1036–1054.

Thompson, J.C., 1980: A comment on the cause of the diurnal and annual temperature cycles - Reply; *Bull. Amer. Meteor. Soc*, **61(11)**, 1411–1411.

van den Hurk, B.J.J.M, P. Viterbo, and S.O. Los, 2003: Impact of leaf area index seasonality on the land surface evaporation in a general circulation model; *J. Geophys. Res.*, **108(D6)**, 4191, doi:10.1029/2002JD002846.

Wang, B., R. Wu and K.-M. Lau, 2001: Interannual variability of the Asian summer monsoon: Contrast between the Indian and the Western North Pacific-East Asian monsoons; *J. Climate*, **14**, 4073–4090.

Warrilow, D.A., A.B. Sangster, and A. Slingo, 1986: Modeling of land surface processes and their influence on European climate.; *U.K. Met. Office*, Technical Note DCTN 38, 92 pp.

Yang, S., and K.-M. Lau, 1998: Influences of sea surface temperature and ground wetness on

Asian summer monsoon; *J. Climate*, **11**, 3230–3246.

Xie, P., and P. Arkin, 1995: Analyses of Global Monthly Precipitation Using Gauge Observations, Satellite Estimates, and Numerical Model Predictions; *J. Climate*, **9**, 840–858.

Xie, P., and P. Arkin, 1997: Global precipitation: A 17-year monthly analysis based on gauge observations, satellite estimates, and numerical model outputs; *Bull. Am. Meteor. Soc.*, **78**, 2539–2558.

Tables

Table 1. PFTs considered in ORCHIDEE. The right column specifies whether or not for the specified PFT, the LAI dependence from soil temperature is implemented.

	Plant Functional Type	**LAI seasonal cycle**
1	Tropical broad-leaved evergreen	No
2	Tropical broad-leaved raingreen	Yes
3	Temperate needleleaf evergreen	No
4	Temperate broad-leaved evergreen	No
5	Temperate broad-leaved summergreen	Yes
6	Boreal needleleaf evergreen	No
7	Boreal broad-leaved summergreen	Yes
8	Boreal needleleaf summergreen	Yes
9	C3 grass	Yes
10	C4 grass	Yes
11	C3 agriculture	Yes
12	C4 agriculture	Yes

Table 2. JJA mean values of roughness length (Z0) and albedo averaged over 4 regions at T30 resolution for Echam4 and EchOrc. Observed albedo are from ISCCP D1 monthly climatology (1984-2000). The 4 regions are the Indian Summer Monsoon region (ISM, 0-30°N, 70-85°E), the Amazon Basin (15S-7°N 285-310°E), the Equatorial Africa (12S-12°N 10-40°E) and Eurasia (55-65°N 35-120°E). Only continent grid points are used in the area averages.

	ISM		Amazon		Africa		Eurasia	
	Z0(m)	Albedo(-)	Z0(m)	Albedo(-)	Z0(m)	Albedo(-)	Z0(m)	Albedo(-)
Ech4	1.3043	0.1739	2.77127	0.13450	1.4421	0.15604	0.6728	0.15075
EchOrc	1.1007	0.1834	1.1145	0.1273	0.7929	0.1582	0.5344	0.18142
Obs		0.1681		0.12515		0.1764		0.1292

Table 3. JJA values of Bowen ratio (BR) and relative soil wetness (SW) averaged over 4 regions for Echam4 and EchOrc. NCEPII reanalysis Bowen ratios are also reported. The regions selected are the same as in Table 3. Only continent grid points are used in the area average.

	ISM		Amazon		Africa		Eurasia	
	BR(-)	SW(-)	BR(-)	SW(-)	BR(-)	SW(-)	BR(-)	SW(-)
Ech4	0.8152	0.5257	0.4416	0.6311	1.3685	0.6533	0.1193	0.8145
EchOrc	0.1957	0.6838	0.0069	0.5653	0.5221	0.6266	0.1210	0.8600
reanalysis	0.3899		0.1215		0.3695		0.12055	

Table 4. Hydroclimatology for 4 regions as simulated at the different resolutions by Echam4 and EchOrc and as in the observations-reanalysis (CRU data are used for precipitation and NCEP II data for evapotranspiration). All the values reported are in mm/d. P is the averaged Precipitation, E evapotranspiration and -DivQ is the convergence (see text for details). The regions selected are the same of table 3. Only continent grid points are used in the area average.

		ISM			Amazon			Africa			Eurasia		
		$\bar{P}$	$\bar{E}$	$-div\bar{Q}$	$\bar{P}$	$\bar{E}$	$-div\bar{Q}$	$\bar{P}$	$\bar{E}$	$-div\bar{Q}$	$\bar{P}$	$\bar{E}$	$-div\bar{Q}$
Ech4	T30	4.371	2.701	1.907	1.867	2.710	-0.877	2.600	2.095	0.454	1.888	1.787	0.2476
Ech4	T106	4.231	2.456	2.214	2.798	3.165	-0.265	2.728	2.168	0.722	1.573	2.2212	-0.336
EchOrc	T30	5.700	3.328	2.638	3.109	3.971	-0.915	2.798	2.861	0.1061	2.869	2.957	0.2003
EchOrc	T106	5.884	3.386	2.748	3.928	4.328	-0.454	3.279	2.908	0.336	2.515	2.925	-0.283
Reana		6.877	3.409	3.335	4.652	3.673	1.213	3.138	2.894	0.151	2.194	3.615	-1.370

Figure Captions

Fig. 1. Vegetation LAI as simulated by EchOrc (panels a and c) and as represented in the FASIR satellite derived dataset (panels b and d). Upper panels show the JFM climatological mean while lower panels the JJA mean. Below 3 LAI contour interval is 0.5.

Fig. 2. JJA 2 meters temperature (°C) climatology for Echam4 (panel a), EchOrc (panel b) and ERA40 reanalysis (panel c). Below 15 °C contour interval is 5 °C and the dashed lines indicate negative contours. The EchOrc-Echam4 differences are shown in panel d; the plotted values satisfy a t-test for difference of means at the significance level of 5%.

Fig. 3. JJA surface latent heat flux ($\frac{W}{m^2}$; positive downward) climatological mean for Echam4 (panel a), EchOrc (panel b) and NCEPII reanalysis (panel c). The EchOrc-Echam4 differences are shown in panel d; the plotted values satisfy a t-test for difference of means at the significance level of 5%. Panels e and f shows the percentage of surface latent heat flux due respectively to transpiration and to interception loss as simulated by EchOrc.

Fig. 4. JJA total precipitation ($\frac{mm}{d}$) climatological mean for Echam4 (panel a), EchOrc (panel b) and CMAP (panel c). The EchOrc-Echam4 differences are shown in panel d; the plotted values satisfy a t-test for difference of means at the significance level of 5%.

Fig. 5. JJA 850mb wind ($\frac{m}{s}$) climatology for Echam4 (panel a), EchOrc (panel b) and ERA40 reanalysis (panel c). The EchOrc-Echam4 differences are shown in panel d; the plotted values satisfy a t-test for difference of means at the significance level of 5%. The vector scale is reported at the bottom of each panel. The colors further indicate the vector magnitude.

Fig. 6. JJA residual surface heat budget ($\frac{W}{m^2}$) climatological mean for Echam4 at T30 resolution (panel a), Echam4 at T30 resolution but for the experiment with the shorter integration time step

(panel b) and Echam4 at T106 resolution (panel c). The (Ech4-T30 $\Delta t = 720s$) - (Ech4-T30 $\Delta t = 1800s$) differences are shown in panel d; the plotted values satisfy a t-test for difference of means at the significance level of 5%.

Fig. 7. JJA 2 meters temperature (°C) climatological mean for Echam4 at T30 resolution (panel a), Echam4 at T30 resolution but for the experiment with a shorter integration time step (panel b) and Echam4 at T106 resolution (panel c). Below 15 °C contour interval is 5 °C and the dashed lines indicate negative contours. The (Ech4-T30 $\Delta t = 720s$) - (Ech4-T30 $\Delta t = 1800s$) differences are shown in panel d; the plotted values satisfy a t-test for difference of means at the significance level of 5%.

Fig. 8. Difference in JJA mean 2 meters temperature (°C) between simulated fields and ERA40 reanalysis. Panels a and c (b and d) display the results obtained with Echam4 (EchOrc) at T30 and at T106 resolution, respectively. The plotted values satisfy a t-test for difference of means at the significance level of 5%. Only the grid points with significant differences (5% level) between EchOrc and Echam4 simulations are displayed.

Fig. 9. Difference in JJA mean 850mb wind ($\frac{m}{s}$) between simulated fields and ERA40 reanalysis. Panels a and c (b and d) display the results obtained with Echam4 (EchOrc) at T30 and at T106 resolution, respectively. The plotted values satisfy a t-test for difference of means at the significance level of 5%. Only the grid points with significant differences (5% level) between EchOrc and Echam4 simulations are displayed.

Fig. 10. Difference in JJA mean latent heat flux ($\frac{W}{m^2}$; positive downward) between simulated fields and NCEPII reanalysis. Panels a and c (b and d) display the results obtained with Echam4 (EchOrc) at T30 and at T106 resolution respectively. The plotted values satisfy a t-test for difference of means at the significance level of 5%. Only the grid points with significant differences (5% level) between EchOrc and Echam4 simulations are displayed.

Fig. 11. Difference in JJA mean total precipitation ($\frac{mm}{d}$) between simulated fields and CMAP data. Panels a and c (b and d) display the results obtained with Echam4 (EchOrc) at T30 and at T106 resolution respectively. The plotted values satisfy a t-test for difference of means at the significance level of 5%. Only the grid points with significant differences (5% level) between EchOrc and Echam4 simulations are displayed.

Fig. 12. South-east Asian monsoon region (T30 runs): panel a (panel b) shows the JJA mean precipitation difference ($\frac{mm}{d}$) between Echam4 (EchOrc) and CMAP data. Panel c (panel d): JJA mean latent heat flux difference ($\frac{W}{m^2}$; positive downward) between Echam4 (EchOrc) and NCEPII. Panel e (panel f): JJA mean 2 meters temperature difference (°C) between Echam4 (EchOrc) and ERA40. The plotted values satisfy a t-test for difference of means at the significance level of 5%. Only the grid points with significant differences (5% level) between EchOrc and Echam4 simulations are displayed.

Fig. 13. South-east Asian monsoon region (T106 runs): panel a (panel b) shows the JJA mean precipitation difference ($\frac{mm}{d}$) between Echam4 (EchOrc) and CMAP data. Panel c (panel d): JJA mean latent heat flux difference ($\frac{W}{m^2}$; positive downward) between Echam4 (EchOrc) and NCEPII. Panel e (panel f): JJA mean 2 meters temperature difference (°C) between Echam4 (EchOrc) and ERA40. The plotted values satisfy a t-test for difference of means at the significance level of 5%. Only the grid points with significant differences (5% level) between EchOrc and Echam4 simulations are displayed.

Fig. 14. Indian summer monsoon region (0-30°N, 70-85°E): climatological seasonal cycle of the IMI index (panels a and f), continents only precipitation (panels b and g), continents only temperature at 2 meters (panels c and h), continents only surface-to-atmosphere moisture flux (panels d and i) and continents only atmospheric moisture convergence (panels e and l). The dot-dashed lines are for the EchOrc simulations, the dashed for Echam4 and the solid ones for observations/reanalyses. Left panels refer to T30 simulations and right panels to the T106 results.

Figures

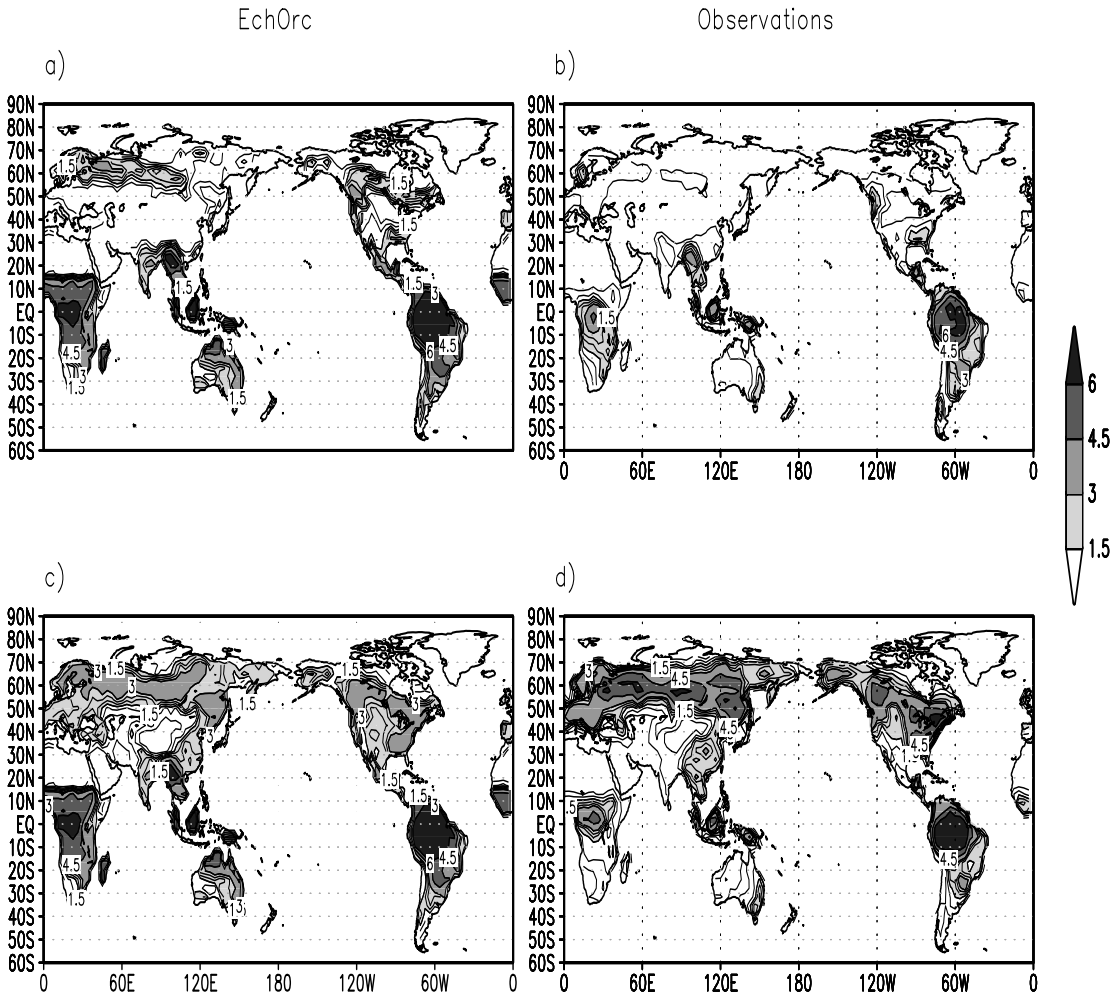

Fig. 1. Vegetation LAI as simulated by EchOrc (panels a and c) and as represented in the FASIR satellite derived dataset (panels b and d). Upper panels show the JFM climatological mean while lower panels the JJA mean. Below 3 LAI contour interval is 0.5.

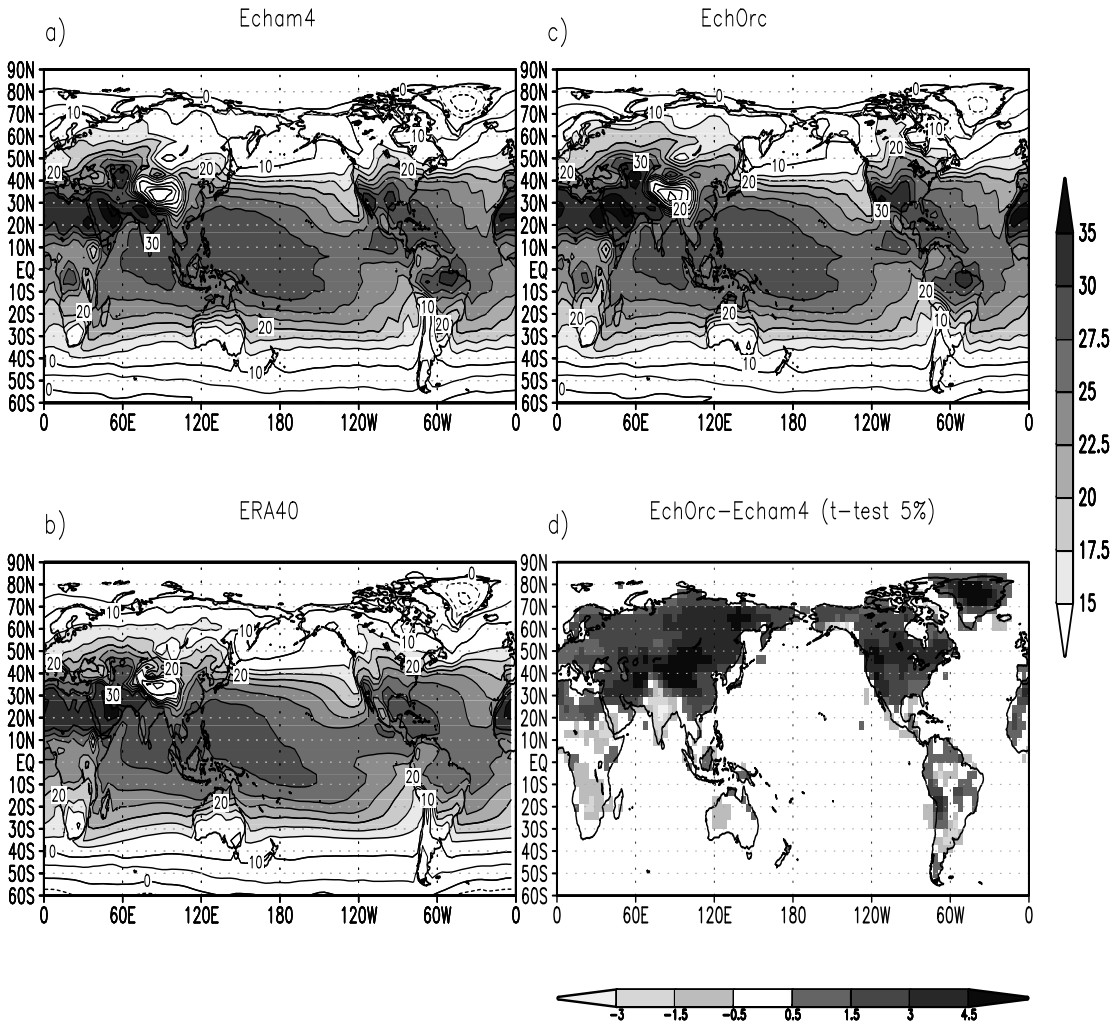

Fig. 2. JJA 2 meters temperature (°C) climatology for Echam4 (panel a), EchOrc (panel b) and ERA40 reanalysis (panel c). Below 15 °C contour interval is 5 °C and the dashed lines indicate negative contours. The EchOrc-Echam4 differences are shown in panel d; the plotted values satisfy a t-test for difference of means at the significance level of 5%.

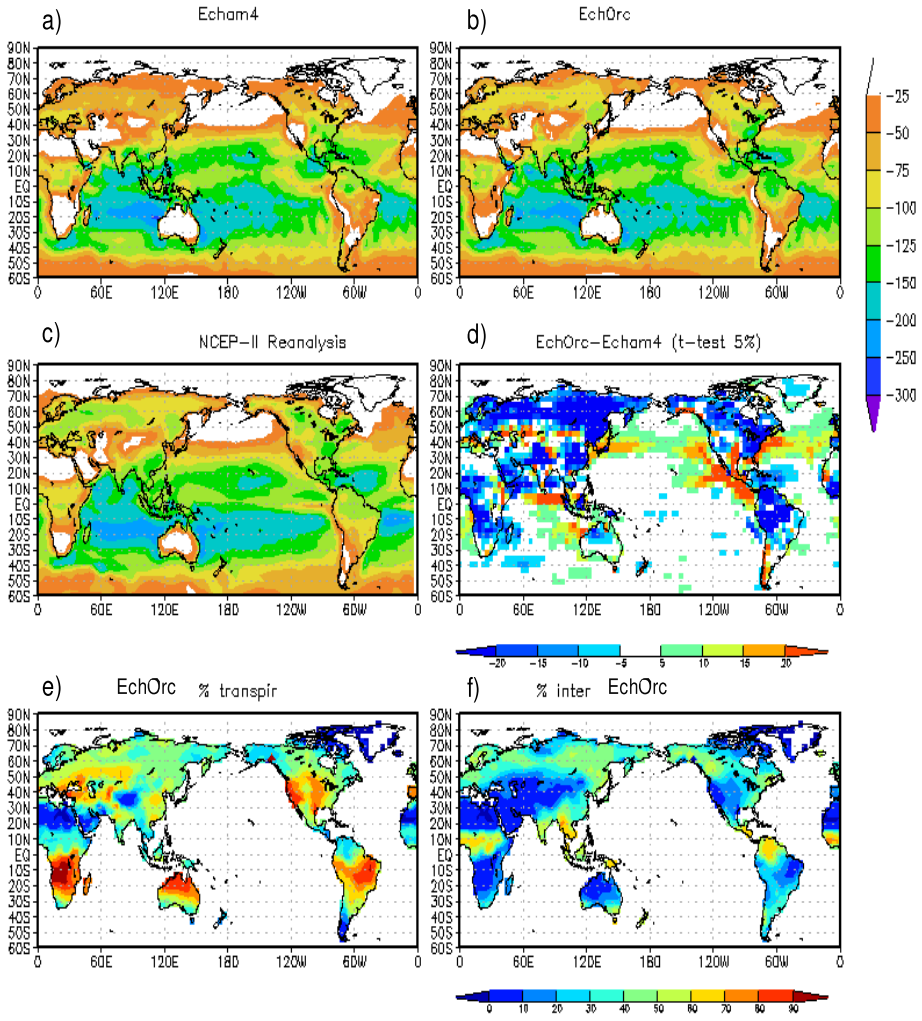

Fig. 3. JJA surface latent heat flux ($\frac{W}{m^2}$; positive downward) climatological mean for Echam4 (panel a), EchOrc (panel b) and NCEPII reanalysis (panel c). The EchOrc-Echam4 differences are shown in panel d; the plotted values satisfy a t-test for difference of means at the significance level of 5%. Panels e and f shows the percentage of surface latent heat flux due respectively to transpiration and to interception loss as simulated by EchOrc.

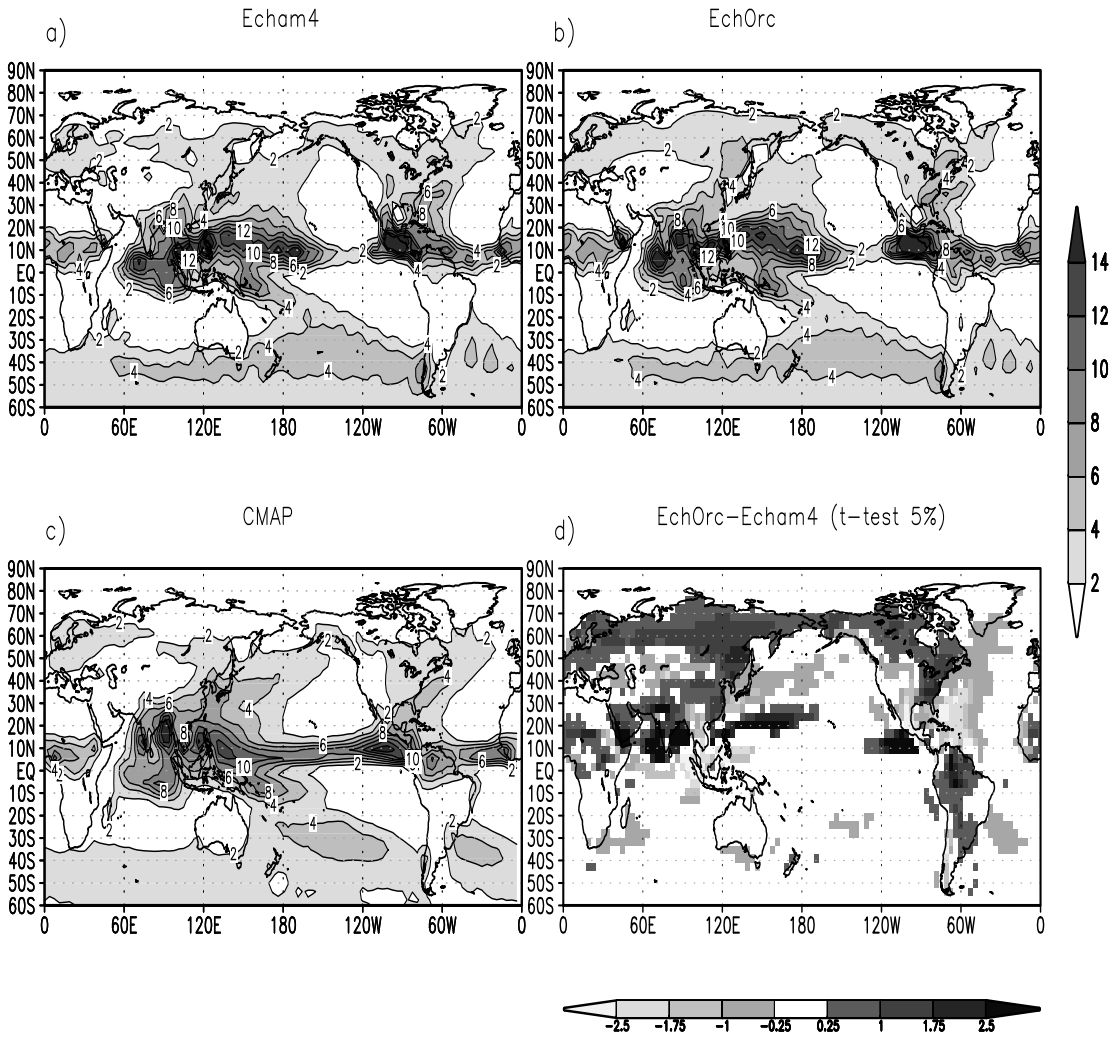

Fig. 4. JJA total precipitation ($\frac{mm}{d}$) climatological mean for Echam4 (panel a), EchOrc (panel b) and CMAP (panel c). The EchOrc-Echam4 differences are shown in panel d; the plotted values satisfy a t-test for difference of means at the significance level of 5%.

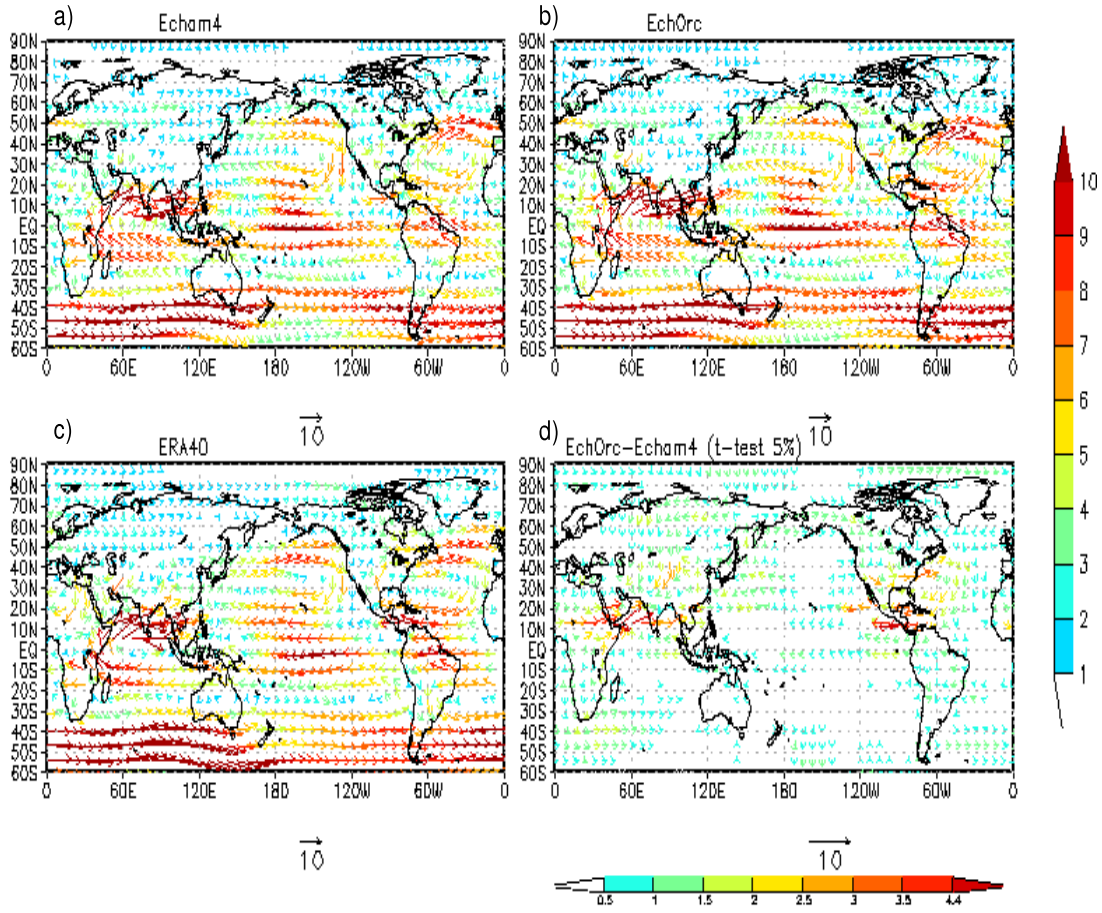

Fig. 5. JJA 850mb wind ($\frac{m}{s}$) climatology for Echam4 (panel a), EchOrc (panel b) and ERA40 reanalysis (panel c). The EchOrc-Echam4 differences are shown in panel d; the plotted values satisfy a t-test for difference of means at the significance level of 5%. The vector scale is reported at the bottom of each panel. The colors further indicate the vector magnitude.

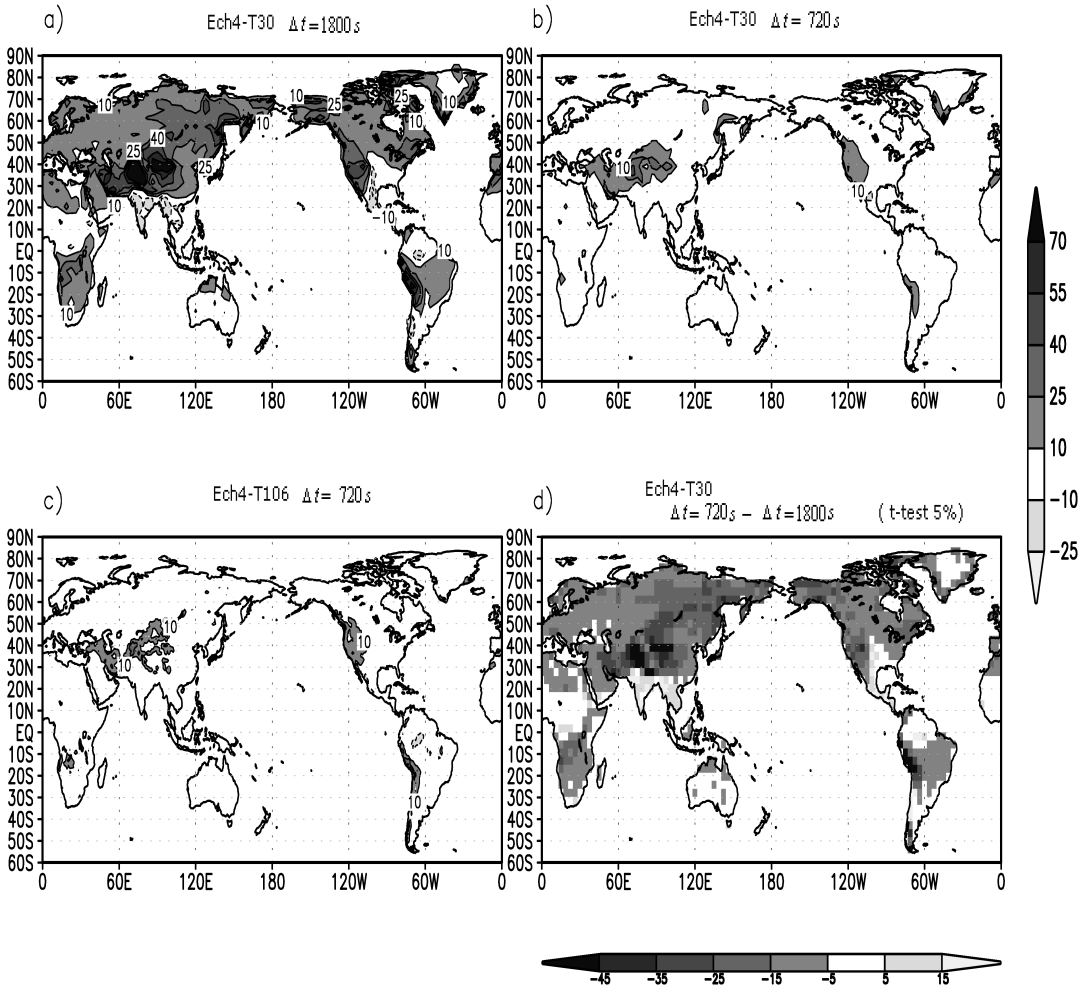

Fig. 6. JJA residual surface heat budget ($\frac{W}{m^2}$) climatological mean for Echam4 at T30 resolution (panel a), Echam4 at T30 resolution but for the experiment with the shorter integration time step (panel b) and Echam4 at T106 resolution (panel c). The (Ech4-T30 $\Delta t = 720s$) - (Ech4-T30 $\Delta t = 1800s$) differences are shown in panel d; the plotted values satisfy a t-test for difference of means at the significance level of 5%.

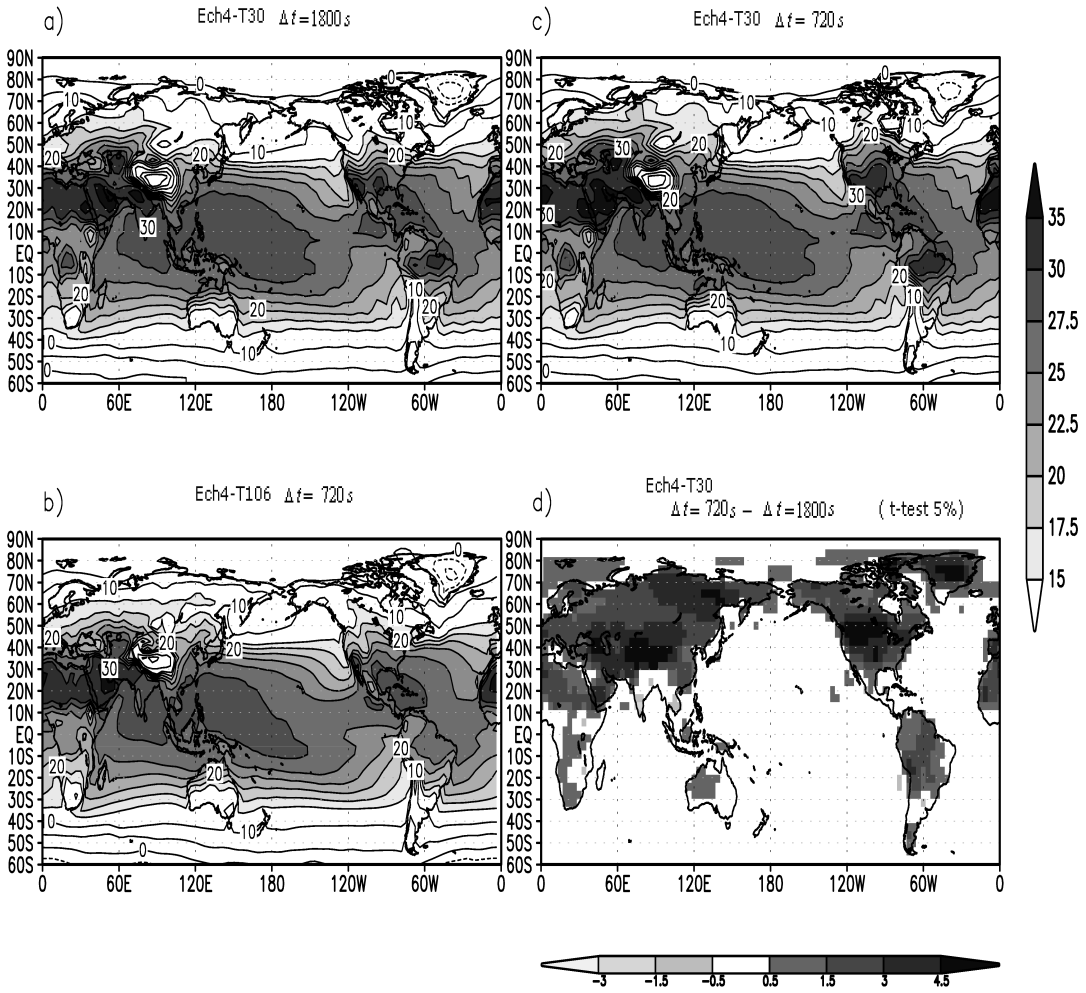

Fig. 7. JJA 2 meters temperature (°C) climatological mean for Echam4 at T30 resolution (panel a), Echam4 at T30 resolution but for the experiment with a shorter integration time step (panel b) and Echam4 at T106 resolution (panel c). Below 15 °C contour interval is 5 °C and the dashed lines indicate negative contours. The (Ech4-T30 $\Delta t = 720s$) - (Ech4-T30 $\Delta t = 1800s$) differences are shown in panel d; the plotted values satisfy a t-test for difference of means at the significance level of 5%.

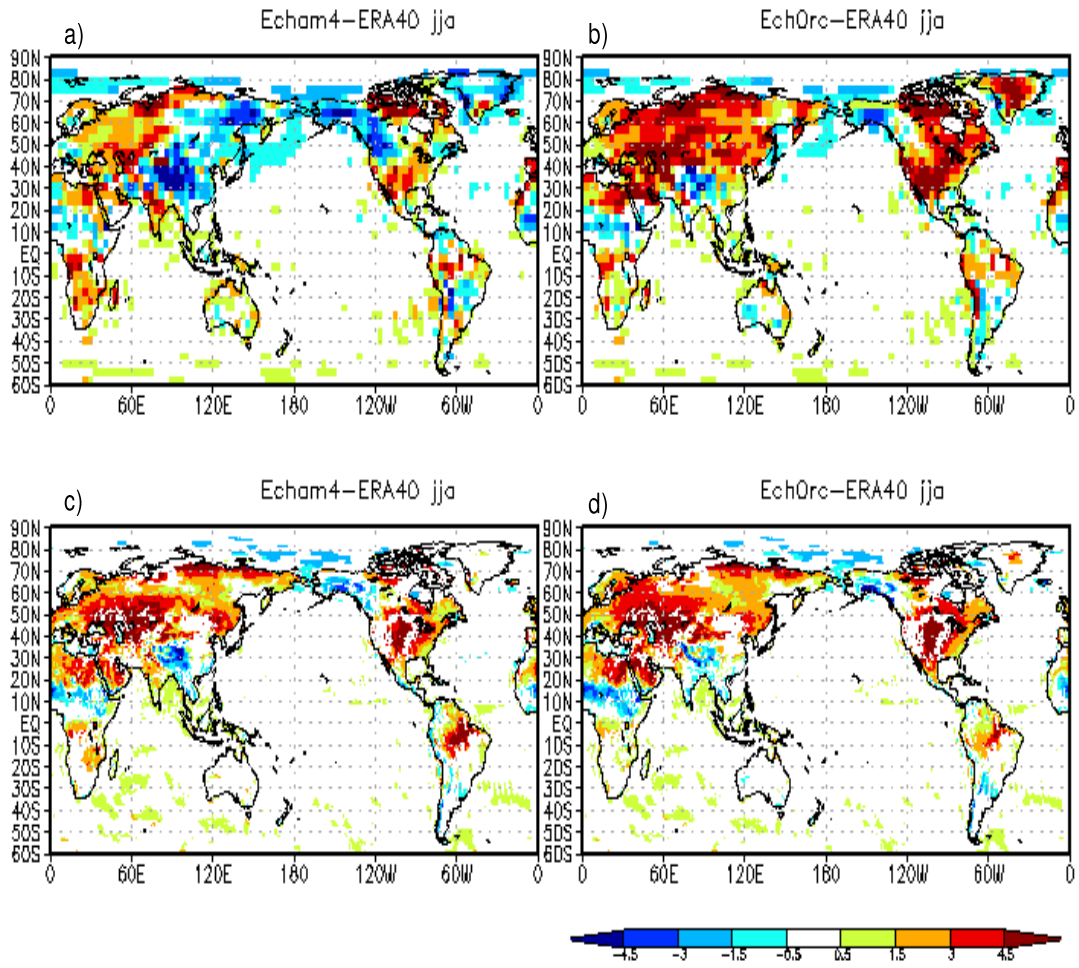

Fig. 8. Difference in JJA mean 2 meters temperature (°C) between simulated fields and ERA40 reanalysis. Panels a and c (b and d) display the results obtained with Echam4 (EchOrc) at T30 and at T106 resolution, respectively. The plotted values satisfy a t-test for difference of means at the significance level of 5%. Only the grid points with significant differences (5% level) between EchOrc and Echam4 simulations are displayed.

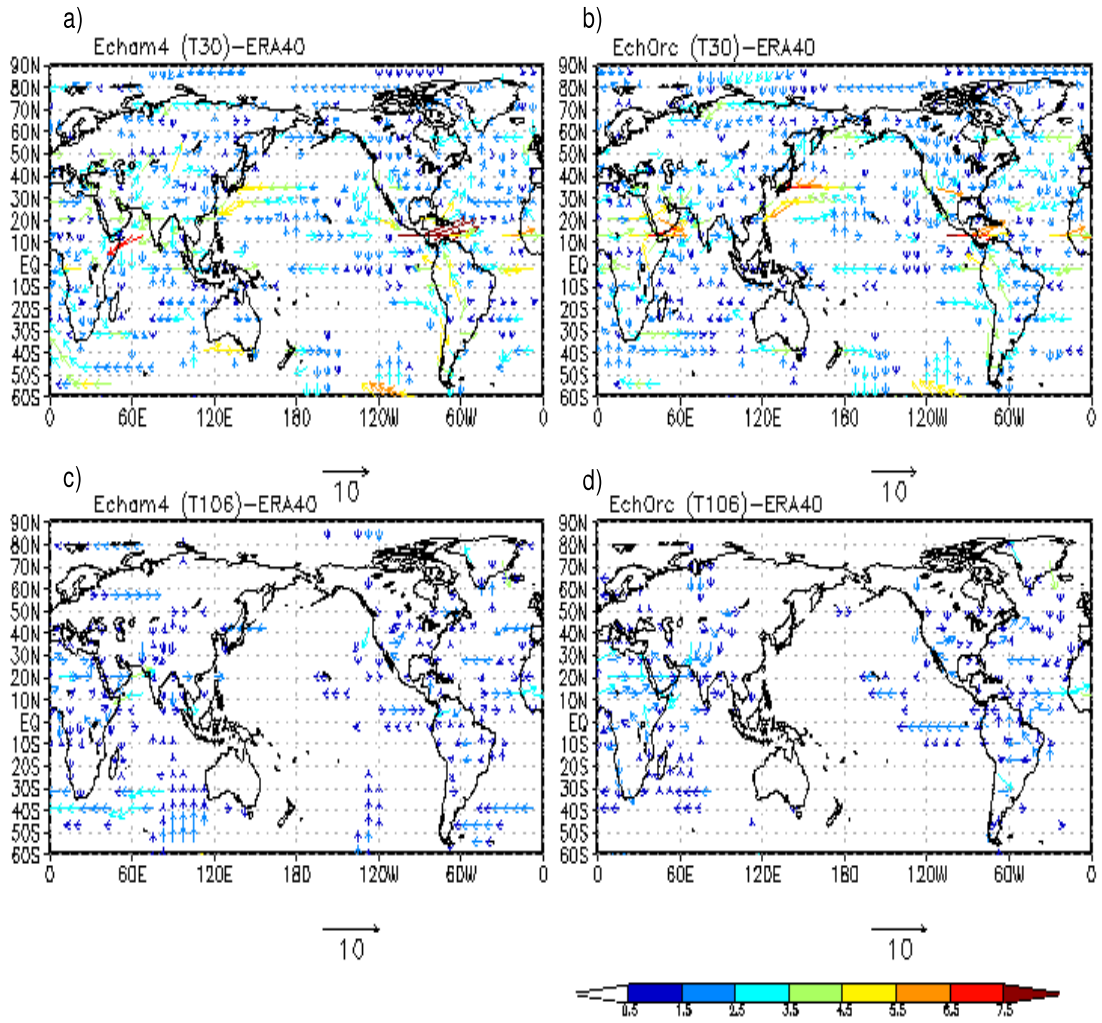

Fig. 9. Difference in JJA mean 850mb wind ($\frac{m}{s}$) between simulated fields and ERA40 reanalysis. Panels a and c (b and d) display the results obtained with Echam4 (EchOrc) at T30 and at T106 resolution, respectively. The plotted values satisfy a t-test for difference of means at the significance level of 5%. Only the grid points with significant differences (5% level) between EchOrc and Echam4 simulations are displayed.

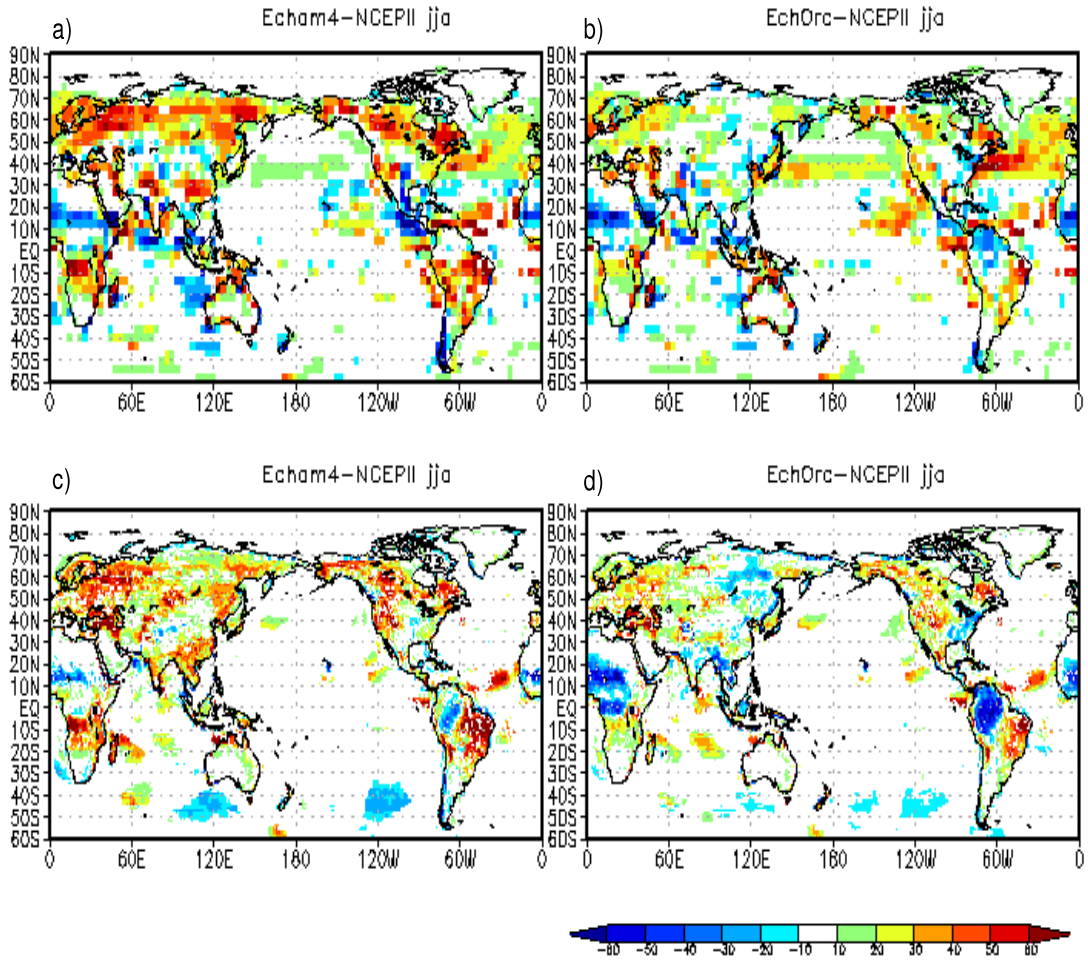

Fig. 10. Difference in JJA mean latent heat flux ($\frac{W}{m^2}$; positive downward) between simulated fields and NCEPII reanalysis. Panels a and c (b and d) display the results obtained with Echam4 (EchOrc) at T30 and at T106 resolution respectively. The plotted values satisfy a t-test for difference of means at the significance level of 5%. Only the grid points with significant differences (5% level) between EchOrc and Echam4 simulations are displayed.

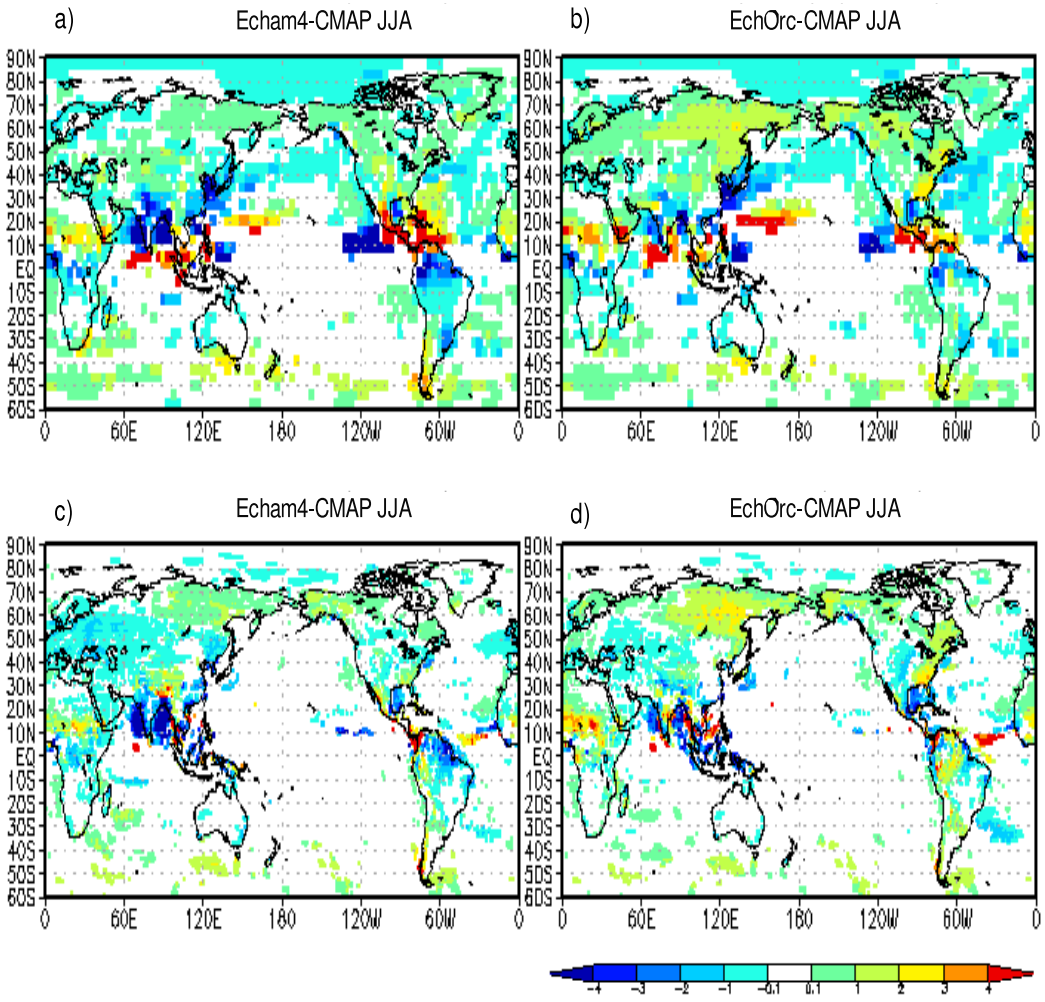

Fig. 11. Difference in JJA mean total precipitation ($\frac{mm}{d}$) between simulated fields and CMAP data. Panels a and c (b and d) display the results obtained with Echam4 (EchOrc) at T30 and at T106 resolution respectively. The plotted values satisfy a t-test for difference of means at the significance level of 5%. Only the grid points with significant differences (5% level) between EchOrc and Echam4 simulations are displayed.

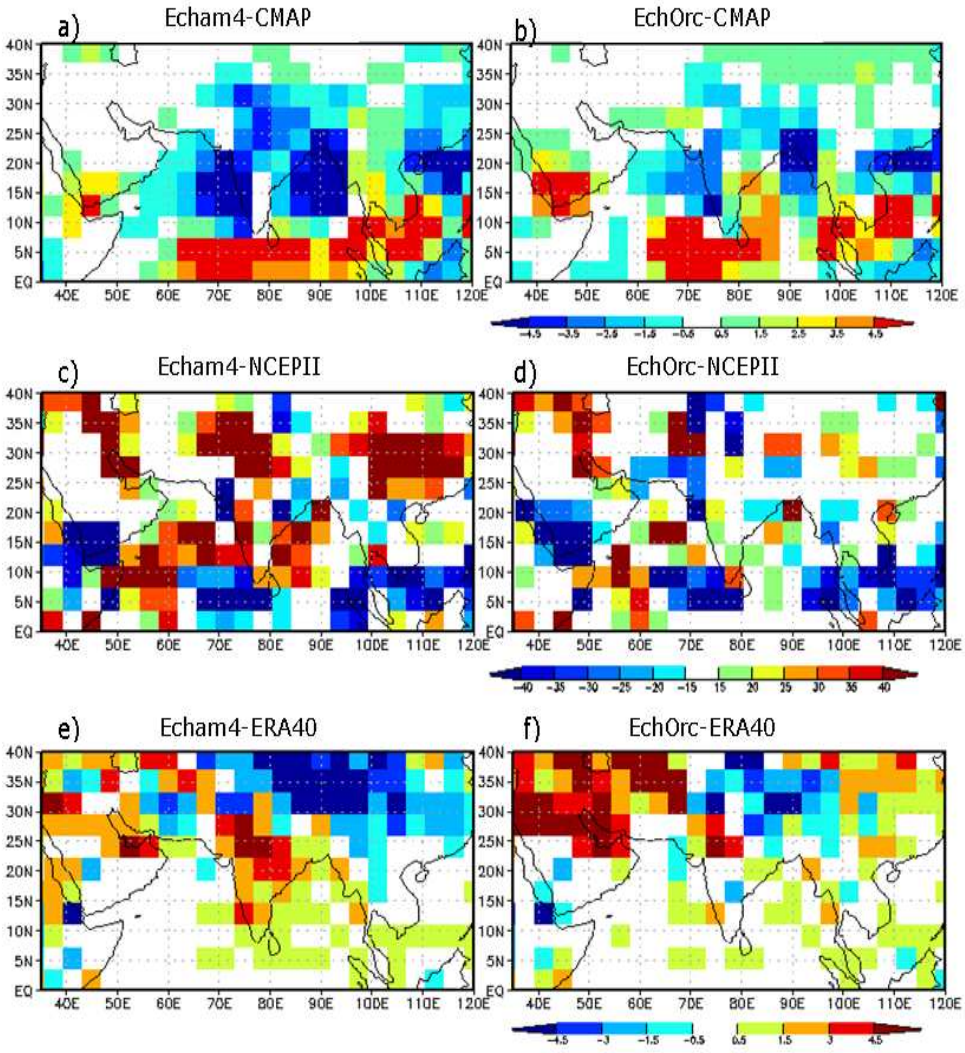

Fig. 12. South-east Asian monsoon region (T30 runs): panel a (panel b) shows the JJA mean precipitation difference ($\frac{mm}{d}$) between Echam4 (EchOrc) and CMAP data. Panel c (panel d): JJA mean latent heat flux difference ($\frac{W}{m^2}$; positive downward) between Echam4 (EchOrc) and NCEPII. Panel e (panel f): JJA mean 2 meters temperature difference (°C) between Echam4 (EchOrc) and ERA40. The plotted values satisfy a t-test for difference of means at the significance level of 5%. Only the grid points with significant differences (5% level) between EchOrc and Echam4 simulations are displayed.

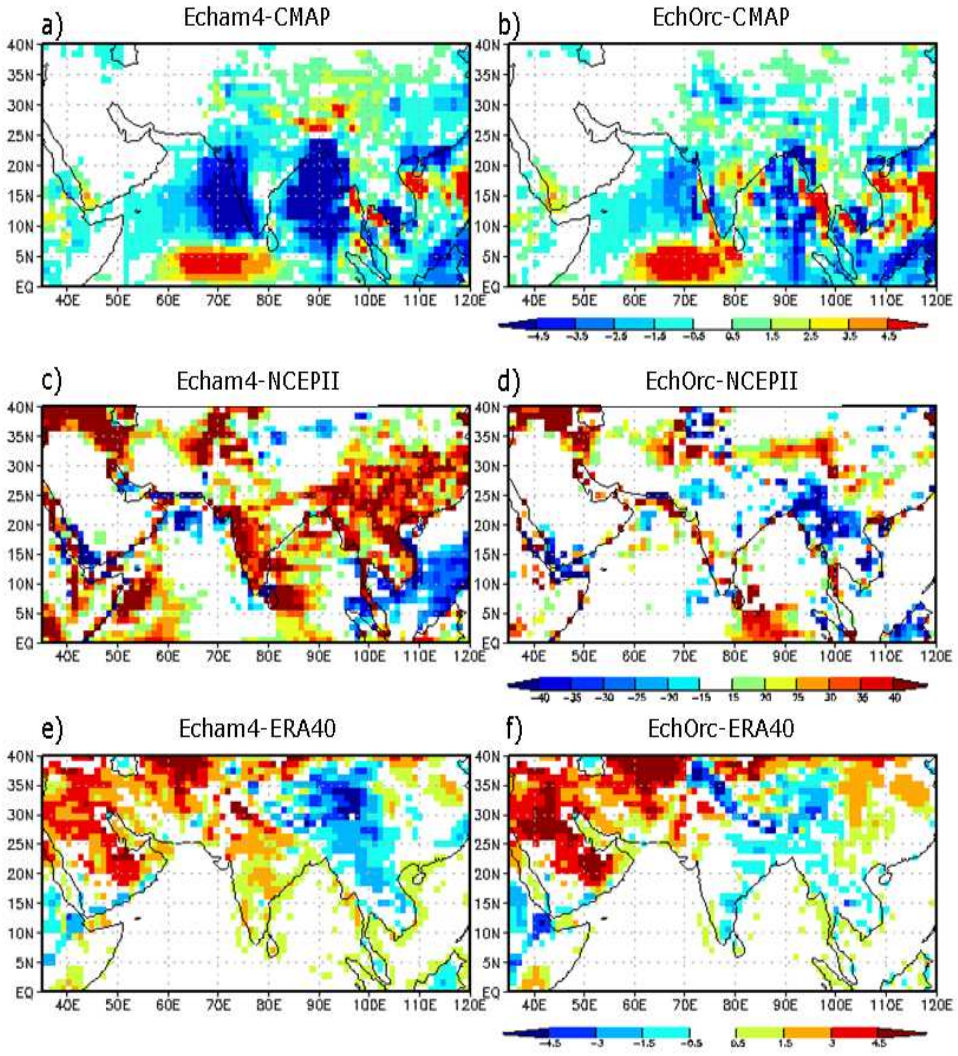

Fig. 13. South-east Asian monsoon region (T106 runs): panel a (panel b) shows the JJA mean precipitation difference ($\frac{mm}{d}$) between Echam4 (EchOrc) and CMAP data. Panel c (panel d): JJA mean latent heat flux difference ($\frac{W}{m^2}$; positive downward) between Echam4 (EchOrc) and NCEPII. Panel e (panel f): JJA mean 2 meters temperature difference (°C) between Echam4 (EchOrc) and ERA40. The plotted values satisfy a t-test for difference of means at the significance level of 5%. Only the grid points with significant differences (5% level) between EchOrc and Echam4 simulations are displayed.

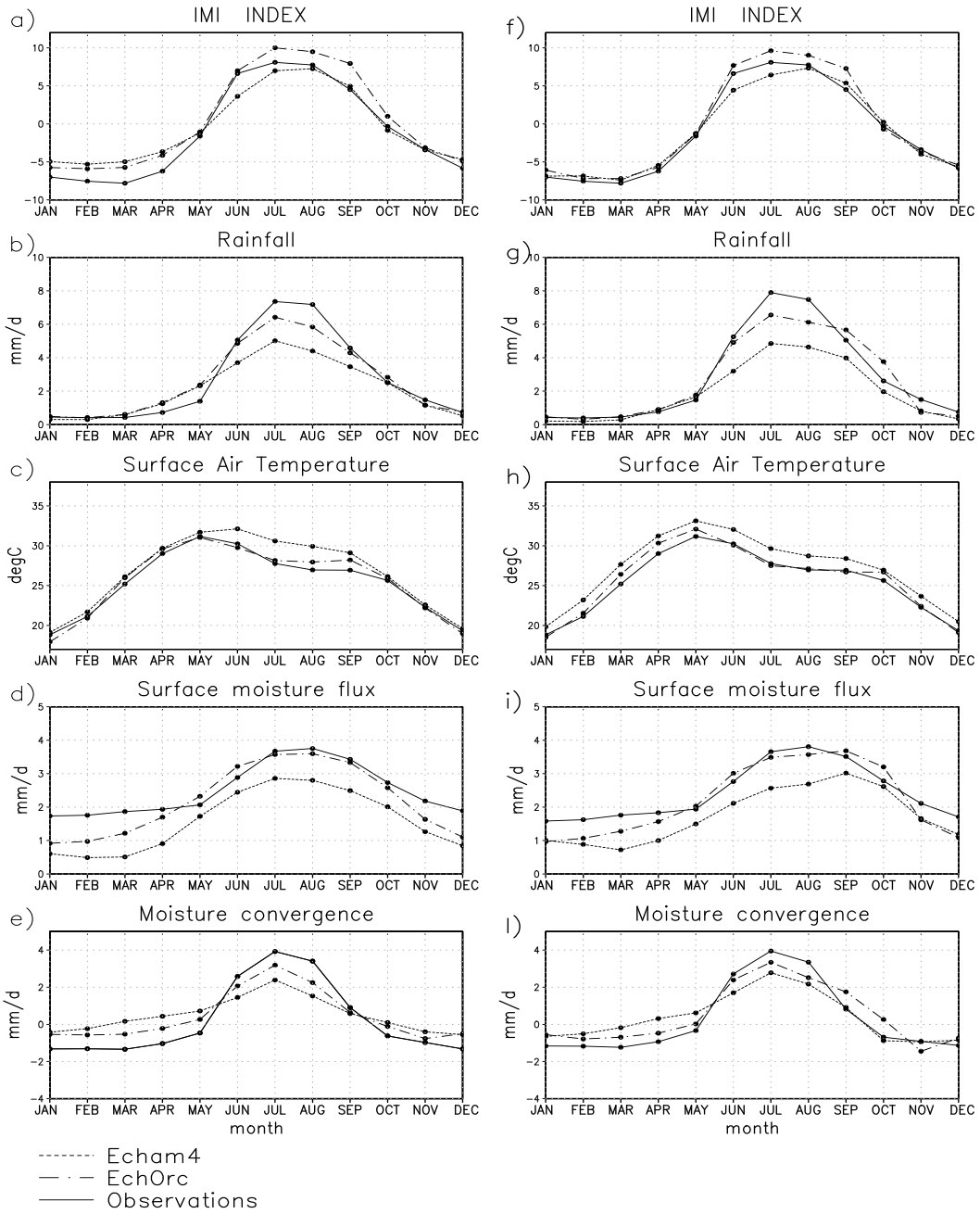

Fig. 14. Indian summer monsoon region (0-30°N, 70-85°E): climatological seasonal cycle of the IMI index (panels a and f), continents only precipitation (panels b and g), continents only temperature at 2 meters (panels c and h), continents only surface-to-atmosphere moisture flux (panels d and i) and continents only atmospheric moisture convergence (panels e and l). The dot-dashed lines are for the EchOrc simulations, the dashed for Echam4 and the solid ones for observations/reanalyses. Left panels refer to T30 simulations and right panels to the T106 results.